MATERIALS SCIENCE

A multimodal defect-rich nanoreactor triggers sono-piezoelectric tandem catalysis and iron metabolism disruption for implant infections

Fuyuan Zheng[1,2]†, Xufeng Wan[1,2]†, Yangming Zhang[1,2]†, Yan Yue[1,2], Qiaochu Li[3], Zhuang Zhang[1,2], Shuoyuan Li[1,2], Hong Xu[1,2], Qiang Su[4], Xiaoting Chen[5], Le Tong[6,7], Long Zhao[1,2], Jian Cao[1,2], Xin Tang[1,2], Xiao Yang[8], Jiagang Wu[9], Jian Li[1,2], Xiang Lv[9]*, Zongke Zhou[1,2]*, Duan Wang[1,2]*

Tracking and eradicating drug-resistant bacteria are critical for combating implant-associated infections, yet effective antibacterial therapies remain elusive. Herein, we propose an oxygen vacancy–rich $(BiFe)_{0.9}(BaTi)_{0.1}O_{3-x}$ nanoreactor as a piezoelectric sonosensitizer by spatiotemporal ultrasound–driven sono- and chemodynamic tandem catalysis to amplify antibacterial efficacy. The piezoelectric charge carriers under a built-in electric field synchronize the reaction of O_2 and H_2O, efficiently generating H_2O_2. The electron-rich oxygen vacancies modulate the local electronic structure of an Fe site. It facilitates reactive oxygen species generation by piezoelectric electrons and accelerates valence state cycles of Fe(III)/Fe(II) to achieve the sustained maintenance of hydroxyl radicals via H_2O_2/Fe(II)–catalyzed chemodynamic reactions, which lead to bacterial membrane damage. Transcriptomics analysis revealed that intracellular Fe overload induced by excessive Fe(II)-mediated dysregulation of the two-component system disrupts bacterial metabolism, triggering bacterial ferroptosis-like death. Thus, the porous titanium scaffold, engineered with a piezoelectric nanoreactor, demonstrates superior antibacterial efficacy under ultrasound and facilitates osteogenesis via piezoelectric immunomodulation–activated therapy.

INTRODUCTION

Titanium (Ti)–based metal has been extensively used in bone implants because of its benign mechanical properties and excellent biocompatibility (*1*). However, Ti implants also show good biocompatibility with bacteria and induce implant-associated infections (IAIs) (*2*). Managing IAIs requires surgical implant revisions and repeated antibiotic therapy (*3*, *4*). Unfortunately, the effectiveness of these strategies is often hindered by antibiotic-induced antimicrobial resistance and biofilm-induced inhibited drug penetration (*5*, *6*). Moreover, the IAIs may arise at all time points because of the unformed osseointegrated interface on the Ti implant (*7*, *8*). Therefore, it is essential to develop an antibiotic-free therapeutic platform on implant surfaces, which can either disrupt the bacterial biofilm or provide effective antimicrobial effects until the complete formation of an osseointegrated interface as needed (*9*, *10*).

Bacterial dynamic therapy is an antibacterial strategy that involves chemical reactions to generate reactive oxygen species (ROS), including photodynamic therapy, sono-piezodynamic therapy (SPT), and chemodynamic therapy (CDT) (*11*, *12*). SPT is a clinical nonantibiotic and noninvasive treatment based on ultrasound (US)–activated piezoelectric sonosensitizers to generate ROS with water (H_2O) and oxygen (O_2) and induce excessive oxidative stress in tumor or bacteria (*13*). Characterized by a noncentrosymmetric crystal, piezoelectric sonosensitizers enable the conversion of mechanical force into electrical energy, generate polarized charges, and therefore create a built-in electric field (BIEF) under US (*14*). Consequently, the BIEF promotes the separation of carriers and generates activated electrons/holes, producing ROS to trigger SPT-mediated antibacterial efficacy (*15*). However, most piezo-based sonosensitizers indicate unsatisfactory redox reactions and ROS yields because of limited carrier concentration and rapid recombination of excited electron-hole pairs under US (*16*, *17*). In addition, the short lifespan of ROS may further reduce antibacterial efficiency (*18*). Thus, exploring an advanced strategy that can simultaneously generate abundant ROS and extend their activity duration to enhance antibacterial efficacy is still challenging. Combining SPT with CDT on the basis of tandem catalysis, which can convert endogenous H_2O_2 to hydroxyl radicals (•OH) through transition metal catalysts (TMCs), especially an iron (Fe)–based Fenton reaction, involves the sequential catalytic processes and synergistically enhances ROS production and duration (*19*). Therein, Fe-based TMCs, based on valence state interconversion between Fe(III) and Fe(II), have achieved an effective CDT effect. However, CDT is inhibited by the relatively low concentration of H_2O_2 in bacteria (*20*). Moreover, the rate-determining step of conventional Fenton reactions limits the CDT efficiency because of the high activation energy of Fe(III) in H_2O_2 decomposition kinetics (*21*). The piezocatalytic self-cycled Fenton technology that enables the coupling of Fe(II) regeneration and H_2O_2 production into one redox system would ensure sustained •OH generation (*22*). Thus, the key to develop Fe-based TMCs with explosive and sustained ROS yield, under which the SPT and CDT are activated and synergized in a sequential manner on the basis of tandem catalysis, is to promote a faster Fe(III)/Fe(II) cycle and achieve real-time recovery of Fe(II) and in situ synthesis of H_2O_2.

[1]Orthopedic Research Institute and Department of Orthopedics, West China Hospital, Sichuan University, Chengdu 610041, China. [2]Sports Medicine Center, West China Hospital, Sichuan University, Chengdu 610041, China. [3]Department of Orthopedics, First Affiliated Hospital, Chongqing Medical University, Chongqing 400016, China. [4]Department of Orthopedics, Third Hospital of Mianyang, Sichuan Mental Health Center, Mianyang 621000, China. [5]Animal Experimental Center, West China Hospital, Sichuan University, Chengdu 610041, China. [6]Department of Emergency Medicine, West China Hospital, Sichuan University/West China School of Nursing, Sichuan University, Chengdu 610041, China. [7]Disaster Medical Center, Sichuan University, Chengdu 610041, China. [8]National Engineering Research Center for Biomaterials, Sichuan University, Chengdu 610064, China. [9]College of Materials Science and Engineering, Sichuan University, Chengdu 610065, China.
*Corresponding author. Email: lvxiang@scu.edu.cn (X.L.); zongke@126.com (Z.Zho.); wangduan_bone@163.com (D.W.)
†These authors contributed equally to this work.

Defect engineering is a potent strategy to improve piezoelectric and catalytic performance by regulating the crystal lattice and modulating the surface electronic structure (*23*). Oxygen vacancies (OVs) created by doping-defect engineering not only produce holes to promote charge separation and traps to capture excited electrons but also increase the electron density of reaction center atoms (*24*). It can facilitate the reduction of adjacent Fe(III) sites and expedite the Fe(III)/Fe(II) cycles, as well as accelerate the oxygen reduction to improve H_2O_2 yield (*25*, *26*). Therefore, it is anticipated that Fe-based TMCs with tandem catalysis between SPT and CDT could achieve superior antibacterial efficacy via a doping-defect engineering strategy. However, the monotherapeutic biofilm clearance necessitates high exogenous ROS production, which damages normal tissues (*27*). Meanwhile, the escaping planktonic bacteria recolonize and reform a new biofilm after the exogenous treatment withdraws (*28*). Thus, it is crucial to develop a combined moderate treatment strategy that enables biofilm elimination and sustained suppression of biofilm reformation.

Excessive intracellular iron can disrupt iron homeostasis and induce lipid peroxidation–related bacterial ferroptosis-like death (*29*). However, the bacterial ferroptosis-like death is severely restricted by adaptive defensive pathways to avoid iron accumulation (*30*). Two-component systems (TCSs), as a signal transduction system, not only enable the misfolded metal iron removal but also signal into the pathogens to promote a defense response (*31*). The Fe(II) accumulation can inactivate the defensive efficacy of TCSs and disrupt iron homeostasis, resulting in iron-induced toxicity in pathogens. However, this targeting metal homeostasis strategy may exhibit limited efficacy because of the instability and easy exhaustion of Fe(II) and iron efflux system (*32*). In our previous study, we proposed copper-based sonosensitizers to achieve US-activated piezo-hot carriers that facilitate the Cu(I) conversion, ultimately leading to cuproptosis-like bacterial death (*33*). On the basis of the existing research and hypotheses, the controlled redox state of Fe, induced by spatiotemporal US–driven tandem catalysis and continuous Fe(III)/Fe(II) cycles and Fe(II) conversion, could facilitate TCS-mediated iron metabolic interference and bacterial ferroptosis-like death. However, the ROS-mediated oxidative stress may induce persistent inflammation and impede bone remodeling (*34*). The key to addressing IAIs after bacterial clearance is to relieve inflammation and foster osteogenesis simultaneously (*35*). Piezoelectric materials can create a bioelectrical microenvironment, which targets electrical signals to regulate macrophage behaviors and promote bone regeneration (*36*). By modulating the M1-to-M2 polarization of macrophages, this bioelectrical environment can effectively reshape the inflammatory response and stimulate the expression of osteogenesis-related factors (*37*).

Herein, we prepared a multifunctional Ba/Ti–doped perovskite–structured [$(BiFe)_{0.9}(BaTi)_{0.1}O_{3-x}$ (BFBT)] nanoreactor as a piezoelectric sonosensitizer for combating IAIs through spatiotemporal US–triggered superior antibacterial effects combined with enhanced osteogenesis effects. We developed a BFBT nanocrystal with sufficient OVs using a facile doping-defect engineering strategy. Subsequently, the porous titanium bone implants, commonly used in orthopedic surgery, were modified by integrating BFBT and hydroxyapatite (HA) to create the TH-BFBT scaffold (Fig. 1A). US stimulation can induce the external periodic pressure, produce a polarization change, and therefore create BIEF in the nanoreactor. Specifically, the more negative and positive redox potential levels in BFBT allowed the separated charge carriers to react with O_2 and H_2O, promoting piezocatalytic H_2O_2 and ROS synthesis under US. Meanwhile, the OVs enabled electron migration to the Fe site driven by BIEF during the US process, accelerating valence state cycles of Fe(III)/Fe(II) and sustaining high levels of Fe(II). In situ H_2O_2 could react with Fe(II) to promote efficient CDT, indicating a potential mechanism for tandem catalysis between SPT and CDT, which ultimately induced bacterial elimination regardless of the rate-limiting step and H_2O_2 levels (Fig. 1B). Moreover, the membrane fluidity and permeability induced by ROS could promote the intracellular flux of Fe(II). Transcriptomics analysis revealed that intracellular Fe overload induced by Fe(II)-mediated TCS dysregulation disrupted bacterial metabolism and eliminated bacteria by the combination of sono-piezodynamic CDT and bacterial ferroptosis-like death. In addition, the TH-BFBT scaffold expedited inflammation relieving and bone regeneration by modulating macrophage behavior within an electrical microenvironment and releasing P and Ca ions from HA (Fig. 1C). The multifunctional BFBT coating on the bone implant surface can effectively eliminate bacteria, inhibit potential recurrence by US-driven tandem catalysis therapy between SPT and CDT and TCS-mediated iron metabolic interference therapy, and promote bone regeneration by piezoelectric immunomodulation–activated therapy, marking a notable advancement in IAIs.

RESULTS

Structure of BFBT nanocrystals

The methodology for preparing BFBT is illustrated in Fig. 1A. The transmission electron microscopy (TEM) images displayed irregular particle sizes ranging from 50 to 200 nm in both $BiFeO_{3-x}$ (BF) and BFBT samples, with uniform distribution of all elements confirmed by elemental mapping (Fig. 2A and figs. S1 and S2). High-resolution TEM (HR-TEM) images revealed distinct and orderly lattice fringes in both samples (Fig. 2B). The BF sample displayed an interplanar spacing (*d*) of 0.2866 nm, while the BFBT sample demonstrated a larger *d* value of 0.3044 nm, likely due to the increased length of the metal-oxygen bond and suggesting a degraded degree of crystallinity. Scanning electron microscopy (SEM) images showed a distinctive microstructure in BF and BFBT samples, with nanosized particles adhering to irregular particles (fig. S3), enhancing the surface area for catalytic reactions. X-ray diffraction (XRD) patterns of BF and BFBT displayed a hexagonal crystal structure within the *R*3*c* space group (JCPDS: 75-6667) (Fig. 2C). Although it had the well-known difficulty in synthesizing a pure phase, BFBT had fewer impurity peaks compared to BF, indicating that BFBT had a purer perovskite crystal structure. In addition, the increased intensity of the (006) peak suggested an unfavored crystal orientation, implying that doping-defect engineering influenced the growth of lattice planes (fig. S4). Raman spectroscopy effectively captured the bonding interactions among ions and groups in a perovskite crystal (*38*). The BFBT sample exhibited a shift to a lower wavenumber (redshift) compared to the BF sample (fig. S5). This redshift indicated weakened metal-oxygen bonds, which correlated with the larger *d* value observed using HR-TEM. Subsequently, the distinctive peaks falling within the wavenumber range of 150 to 400 cm^{-1} were subjected to further analysis, as they correspond to the vibrations of B─O bonds, primarily reflecting the vibrations of B-site ions (Fig. 2D). The redshift in the A_1-2 and A_1-3 modes suggested weaker B─O bonds in the BFBT sample, indicating an increased off-center shift of B-site ions and reduced crystallinity (*39*). This weakening was attributed to

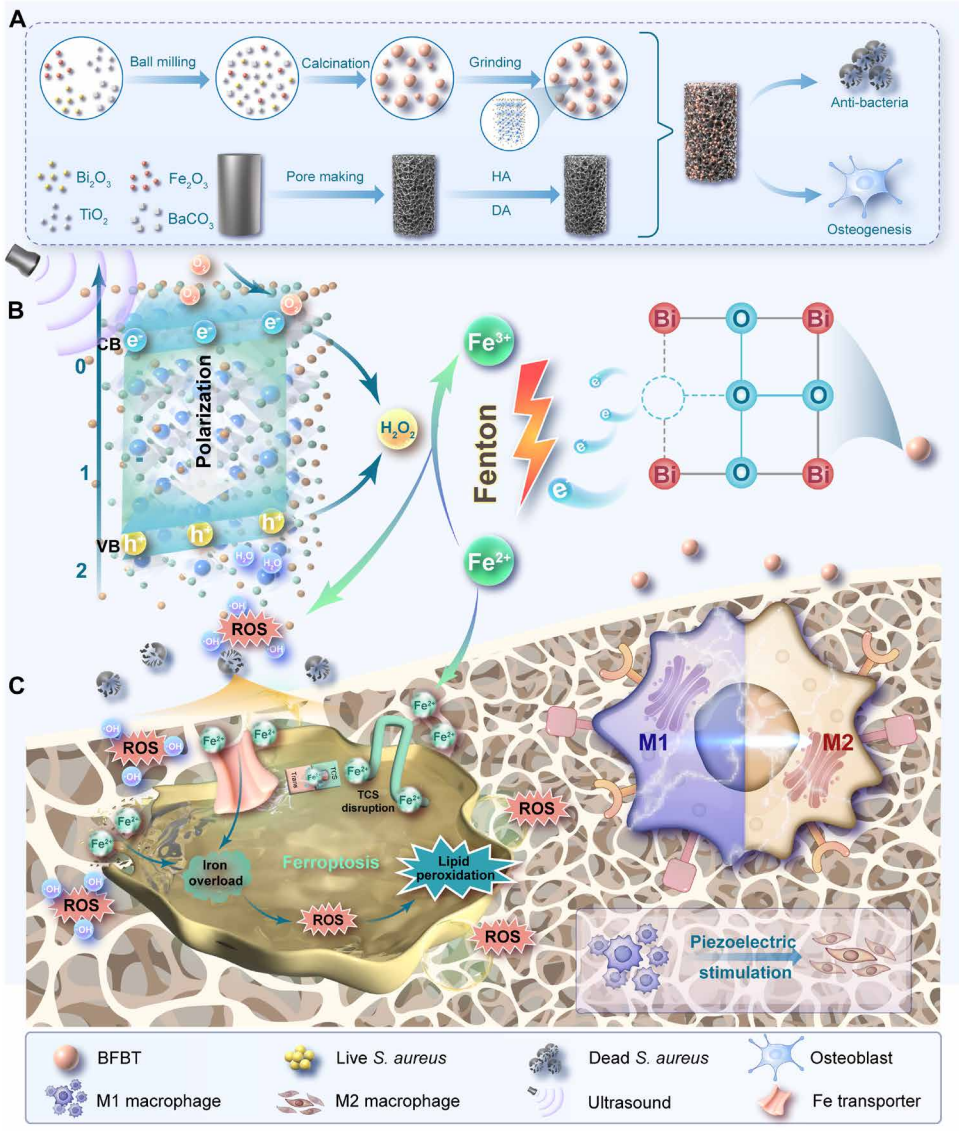

Fig. 1. Schematic illustration of sono-piezoelectric tandem catalysis and bacterial iron metabolism disruption for implant infections. (**A**) Fabrication of BFBT and the TH-BFBT bone scaffold. (**B**) Activated by US, BFBT uses H_2O and O_2 to produce H_2O_2, which subsequently undergoes Fenton reaction. Under BIEF, electron-rich OVs modulated the electron density of adjacent Fe, facilitating the Fe(III)/Fe(II) redox cycle. (**C**) In an infected bone implant model, the TH-BFBT bone scaffold demonstrated antibacterial efficiency through ROS attacks, bacterial ferroptosis-like death, and osteogenesis efficiency by immunomodulation.

the limited hybridization between the oxygen p-orbitals and Fe^{3+}/Ti^{4+} d-orbitals, likely due to the nanodomain formation because of Ba^{2+} and Ti^{4+} doping. Moreover, the full width at half maximum (FWHM) observed in Raman spectroscopy was a significant metric for assessing the symmetry of the BO_6 octahedron. The FWHM of A_1-2 and E-2 modes increased, indicating an enhanced structural disorder and increased local heterogeneity (fig. S6). The increased displacement of B-site ions and greater lattice deformation can enhance piezoelectricity and strain response. Then, we conducted second harmonic generation (SHG) tests on the BF and BFBT samples to assess potential enhancements in piezoelectricity. SHG is frequently used to evaluate the symmetry and piezoelectric properties of piezoelectrics (*40*). The oscilloscope traces of SHG signals at 532 nm for both BF and BFBT samples were illustrated, indicating the existence of piezoelectricity (*41*). The SHG pole figure demonstrated a higher degree of anisotropy in the BFBT sample, suggesting its better piezoelectric response (Fig. 2E and fig. S7).

Piezocatalytic activities of BFBT nanocrystals

To assess the piezocatalytic effect, we measured the generation of •OH and $•O_2^-$. Methylene blue (MB) scavenged •OH, leading to a decrease in absorption intensity (fig. S8) (*42*). The BFBT + H_2O_2 group with US showed the least absorbance, followed by the BF + H_2O_2 group (Fig. 2F). Moreover, prolonged US exposure led to a continuous decline in absorption intensity, confirming the catalytic efficacy of BFBT with H_2O_2 (fig. S9). The generation of $•O_2^-$ was evaluated through the degradation of 1,3-diphenylisobenzofuran (DPBF) (*43*) (fig. S10). There was a notable increase in $•O_2^-$ production

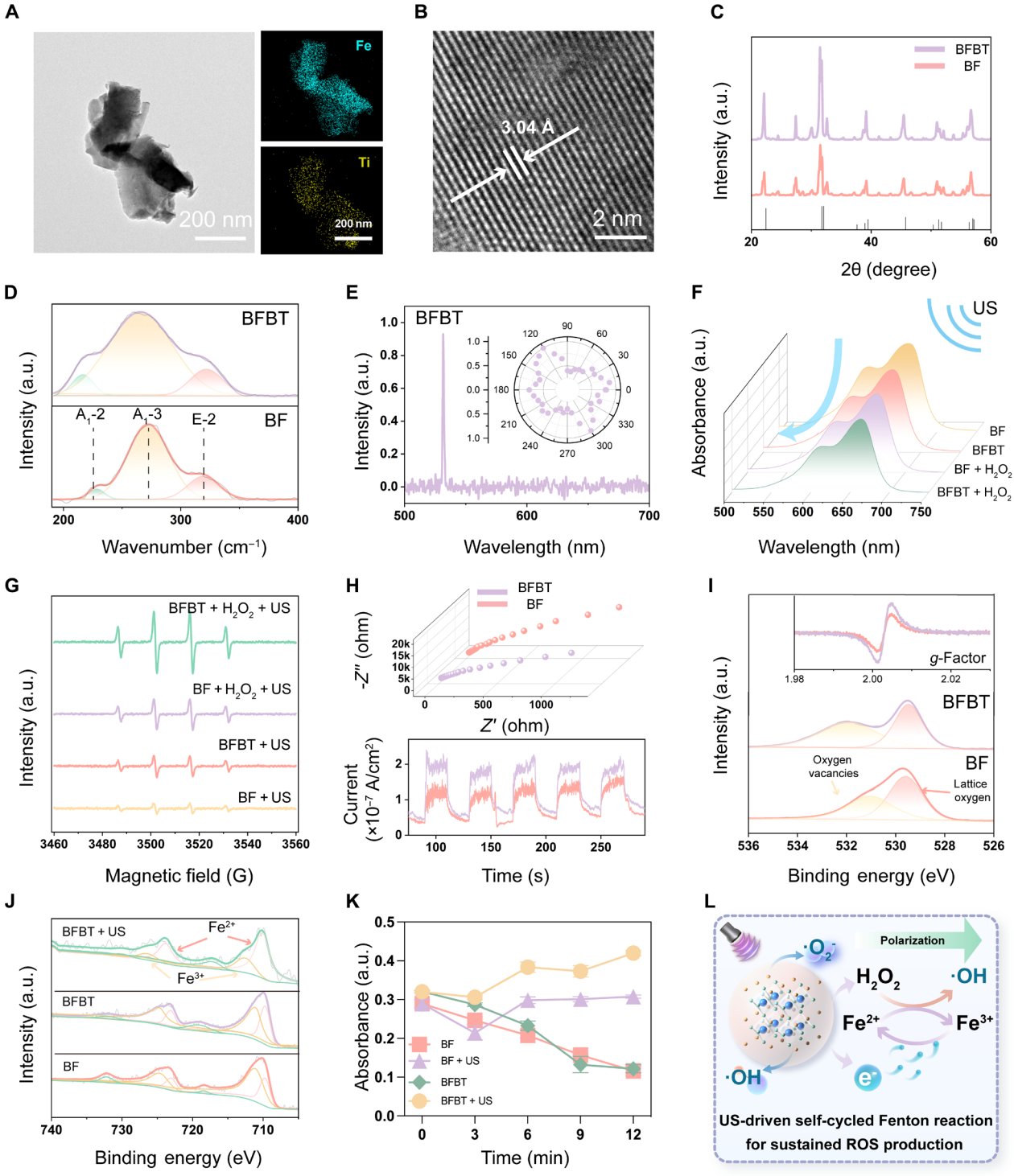

Fig. 2. Structure characterizations and piezocatalytic activities of the BFBT piezocatalyst. (**A**) TEM image and elemental mapping and (**B**) HR-TEM image of the BFBT sample. (**C**) XRD patterns of BF and BFBT samples. a.u., arbitrary units. (**D**) Composition dependence of fitted Raman spectra. (**E**) SHG intensity of the BFBT sample varying with wavelength. (**F**) MB consumptions of different samples under US. (**G**) EPR spectra of •OH. (**H**) EIS Nyquist plots (top) and piezocurrent curves (bottom) of BF and BFBT samples. (**I**) EPR spectra (inset) and narrow-scan XPS spectra of O 1s of BF and BFBT. (**J**) Narrow-scan XPS spectra of Fe 2p. (**K**) Fe(II) concentration fluctuations during the piezocatalytic reaction. (**L**) Mechanism of sustained ROS generation by US-driven self-cycled Fenton reaction with self-supplied H_2O_2 based on BFBT.

observed with the BFBT + US group (fig. S11). To ascertain the specific reactive free radicals involved in our piezocatalysis, we conducted experiments to trap these radicals using various scavengers. These included EDTA [to scavenge Fe(II)], benzoquinone (to scavenge $\bullet O_2^-$), and isopropyl alcohol (to scavenge •OH). Cumulatively, results suggested that •OH predominated as the principal active species, followed by $\bullet O_2^-$ under US. The deficiency of Fe(II) limited the production of •OH, reducing the catalytic efficiency (figs. S12 to S14). To confirm the generation of self-supplied H_2O_2, we used a potassium permanganate–based colorimetric assay. The results demonstrated that both BF and BFBT had the capability to produce H_2O_2 (fig. S15). In addition, electron paramagnetic resonance (EPR) spin-trapping was used to detect •OH generated during piezocatalytic degradation (Fig. 2G). Under US, a quartet peak with a 1:2:2:1 intensity ratio emerged, confirming the formation of DMPO-•OH (*33*). The signal intensity of BFBT was greater than that of BF, and the intensity increased in the presence of H_2O_2. To understand the increased ROS production of BFBT, we initially conducted electrochemical impedance spectroscopy (EIS) and transient piezocurrent spectroscopy (*I-t* curve), as the efficacy of piezocatalytic activity heavily relies on the efficiency of generating, separating, and migrating electron-hole pairs in piezoelectric materials (*17*). The BFBT sample notably displayed smaller semicircle radius in EIS plots than BF, denoting its comparatively lower resistance to charge transfer. Moreover, upon activation of US, the BFBT sample manifested markedly elevated transient piezoelectric current values in *I-t* curves than BF, indicative of a heightened rate of carrier generation (Fig. 2H). It has been reported that facilitated charge transfer and carrier generation were linked to the formation of OVs, which are typically associated with the production of two electrons, implying that increasing concentration of OV (C_{OV}) can enhance electron numbers (*16*). Moreover, the previously mentioned crystallinity degradation caused by doping-defect engineering was anticipated to promote structural relaxation of surface atoms and generate OVs (*44*). Therefore, we investigated OVs using EPR spectra, where BFBT showed a stronger oxygen defect signal at $g = 2.004$, indicating a higher C_{OV} compared to BF (Fig. 2I). The high-resolution XPS spectra of O 1s were fitted by the Lorentz function. The peak at 531 eV is attributed to OV, while the one at 529 eV corresponds to lattice oxygen (*45*). The BFBT sample exhibited a higher C_{OV} of 53.7% compared to the BF sample (fig. S16). Hence, doping-defect engineering not only increased B-site ion displacement to enhance piezoelectricity but also induced structural relaxation and generated OVs, thereby promoting catalytic activities. To further investigate whether OVs influenced the Fe-mediated Fenton reaction, we analyzed the chemical states of Fe using XPS spectra. The rise in the proportion of Fe(II) from 30.5 to 48.0% suggested an increased electron density on Fe within BFBT (Fig. 2J and fig. S17). The elevated Fe(II) content could potentially be attributed to the augmented presence of OVs, which modulated the local electron structure and increased the surrounding electron density of reaction center atoms as electron donors. In addition, our study delved deeper into the status of Fe and OVs in BFBT after 10 min of US treatment. The findings revealed a continued rise in Fe(II), indicating that the piezoelectric potential enhanced the migration of electrons to Fe sites and expedited the Fe(III)/Fe(II) cycles. The slight decrease in C_{OV} suggested that OVs were involved in the piezocatalysis process (fig. S18). To confirm the hypothesis, we undertook an in situ assessment of the Fe(II) content using 1,10-phenanthroline in the reaction solution. Without US, Fe(II) underwent continuous consumption and conversion to Fe(III) with H_2O_2, while under US conditions, the content of Fe(II) remained largely unchanged after the reaction (Fig. 2K). XPS revealed similar results, showing that after reacting with H_2O_2, Fe(II) in BF remained essentially unchanged, whereas in BFBT, the Fe(II) content slightly increased under US (fig. S19). This might be attributed to OVs capturing piezo-electrons under US, thereby increasing local electron density and maintaining Fe(II) levels. For further verification of the sustained Fenton reactions, we monitored the generation of •OH over a continuous 8-hour reaction period, as well as the Fe valence state after the reaction. The EPR results indicated that the production of •OH remained essentially stable throughout 8 hours, and after 8 hours of reaction, ~62.5% of Fe(II) remained on the surface of the BFBT nanoreactor (fig. S20). Therefore, the continuous reduction of Fe(III) to Fe(II) facilitated the piezocatalytic self-cycled CDT, producing •OH with self-supplied H_2O_2 (Fig. 2L).

Mechanistic studies on the enhanced piezocatalytic performance of BFBT nanocrystals

For deeper exploration of the potential in generating ROS under US, the band structures of both BF and BFBT were scrutinized to unveil insights into specific redox reactions. The bandgap was determined by the energies of the conduction band (E_{CB}) and valence band (E_{VB}) (*46*). The bandgap values (E_g) were determined via ultraviolet-visible (UV-vis) diffuse reflectance spectroscopy (fig. S21) and calculated using the Tauc equation

$$(\alpha h\nu)^{1/n} = A\left(h\nu - E_g\right) \quad (1)$$

In the equation, α represents the absorption coefficient, *h* represents the Planck constant, *A* refers to a constant, and *ν* stands for the photon frequency; for direct bandgap semiconductors, *n* is 1/2. The E_g values for BF and BFBT were measured as 1.98 and 2.07 eV, respectively (fig. S22). The Mott-Schottky plots were generated for BF and BFBT to ascertain the E_{CB}, with the flat-band potential (E_{fb}) computed from the linear plot intercept. The positive slope signified the n-type semiconductor for both materials. For BF and BFBT, the determined E_{fb} values were −0.09 and −0.28 V, respectively (versus NHE, 0.22 V more positive versus Ag/AgCl) (fig. S23). For n-type semiconductors, the E_{CB} tends to be 0.1 to 0.2 eV more negative than the E_{fb}. Following rigorous calculations, the E_{CB} values were established as −0.19 and −0.38 eV for BF and BFBT, respectively. The E_{VB} was subsequently determined (Fig. 3A) through the equation

$$E_{VB} = E_{CB} + E_g \quad (2)$$

The inherent CB potential of BFBT was more negative than that of BF, which was negative enough to meet the redox potential of $O_2/\bullet O_2^-$ at −0.33 V, suggesting that the electrons within the CB were favorable for the redox reaction. The E_{CB} of both BF and BFBT fulfilled the criteria for reacting with $\bullet O_2^-/H_2O_2$ (0.35 V) and H_2O_2/•OH (1.49 V). Moreover, the BFBT sample exhibited the greatest piezo-potential and band bending, facilitating faster arrival of free electrons (e^-) and holes (h^+) at the nanocrystal surface to engage in the reaction, thus triggering the tandem redox reaction (Fig. 3B). The bent band of BFBT also met the reaction conditions of H_2O/H_2O_2 (1.76 V). In conclusion, we formulated a mechanism for ROS generation through US-driven sono-piezoelectric tandem catalysis (Eqs. 3 to 7). Furthermore, the larger bandgap of BFBT, combined

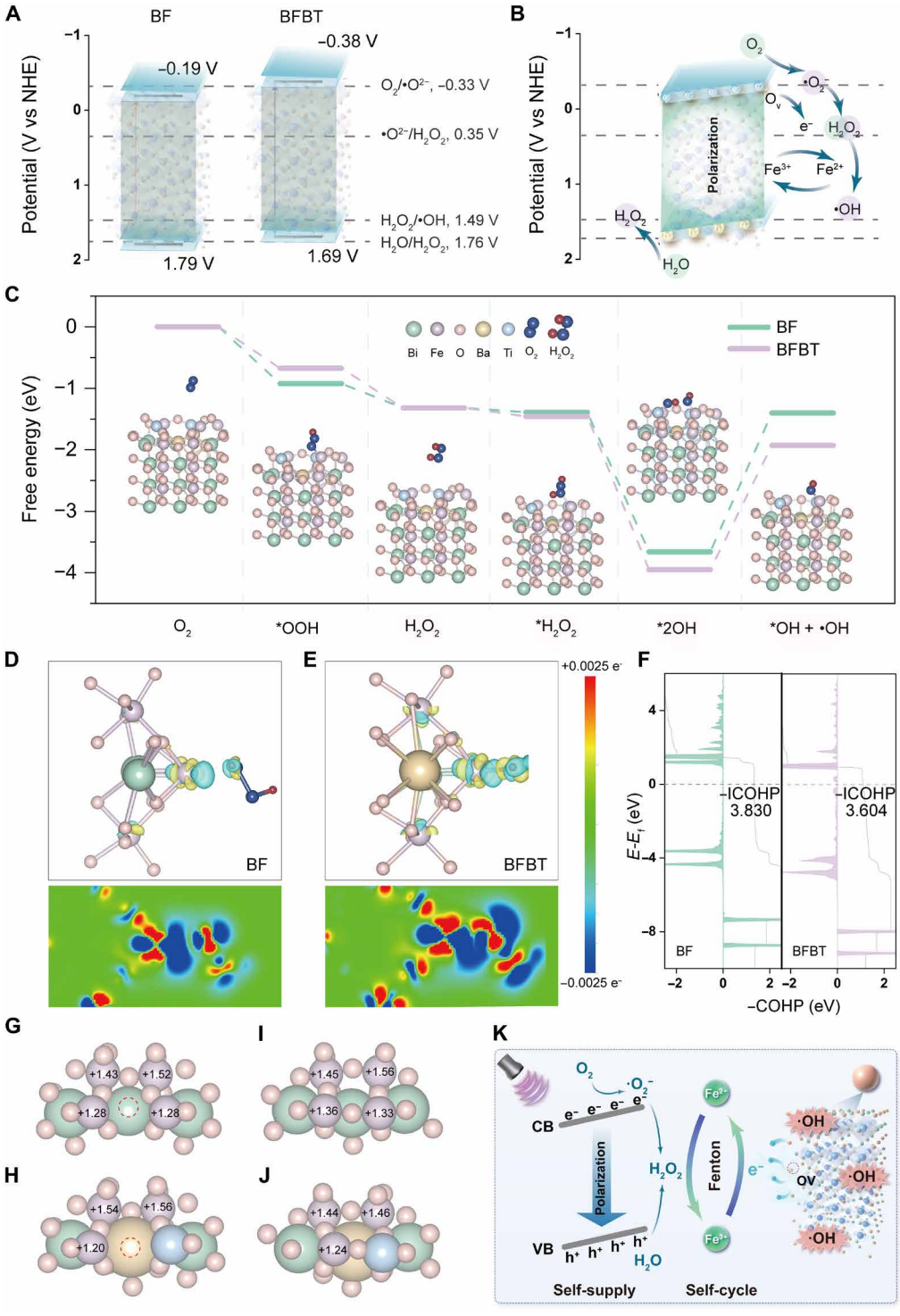

Fig. 3. Mechanism on the piezocatalytic performance of BFBT. (**A**) Band structure diagrams of BF and BFBT samples. (**B**) Tilted band structure of BFBT under US-activated BIEF. (**C**) Energy diagrams and key intermediate conformations of BF and BFBT in tandem reactions. 3D and 2D display of charge density differences of (**D**) BF and (**E**) BFBT. The blue and yellow areas represent charge consumption and accumulation, respectively. (**F**) The COHP curves and ICOHP values for *HOOH on BF and BFBT. Bader charge of Fe around OV of (**G**) BF and (**H**) BFBT. Bader charge of Fe away from OV of (**I**) BF and (**J**) BFBT. (**K**) Mechanism of US-driven sono-piezoelectric tandem catalysis.

with its piezoelectric potential, prevented the recombination of holes and electrons, thereby promoting reaction occurrence.

$$BFBT \longrightarrow e^- + h^+ \quad (3)$$

$$O_2 + e^- \longrightarrow \bullet O_2^- \quad (4)$$

$$\bullet O_2^- + e^- + 2H^+ \longrightarrow H_2O_2 \quad (5)$$

$$H_2O_2 + Fe^{2+} \longrightarrow Fe^{3+} + \bullet OH + OH^- \quad (6)$$

$$2H_2O + 2h^+ \longrightarrow H_2O_2 + 2H^+ \quad (7)$$

To better understand the influential mechanism of enhanced sono-piezoelectric tandem catalysis, we performed density functional theory (DFT) calculations on BF and BFBT. First, we modeled BF and BFBT with OVs wherein the oxygen defect was primarily localized in the surface layers (fig. S24). The corresponding free energy diagrams and key intermediate conformations during the tandem reaction process of generating •OH from O_2 in BF and BFBT simulations were presented (Fig. 3C and fig. S25). The O_2 molecule initially attached to the surfaces of BF and BFBT with reduction energies of −0.92 and −0.67 eV, respectively, revealing that O_2 readily adsorbed on both surfaces and underwent reduction. However, the energy diagram ($U = 0.68$ V) showed that the energy barrier for the step from *OOH to H_2O_2 in BF was too high, resulting in poorer catalytic performance for self-supplied H_2O_2 compared to BFBT (fig. S26). Afterward, Fe* uniformly cleaved the self-supplied H_2O_2 to create surface-active groups that were bound to Fe around OV. Notably, the electron-rich Fe in BFBT exhibited higher reactivity, leading to a strong adsorption capacity, making it challenging for H_2O_2 molecules to stabilize on the surface, thereby directly dissociating into 2OH* with low energy. This demonstrated that electron-rich Fe reduced the energy barrier for H_2O_2 adsorption and dissociation, thereby boosting the activity of Fenton reaction. Moreover, differential charge density analysis revealed a larger electron cloud between BFBT and *HOOH, indicating more substantial electron injection from BFBT to *HOOH compared to BF (Fig. 3, D and E, and fig. S27). In addition, the crystal orbital Hamilton population (COHP) analysis showed a decrease in the negative integrated COHP (−ICOHP) value, indicating that the O—O bond was weaker in *HOOH in BFBT (Fig. 3F). These points provided a robust explanation for the enhanced efficiency of ROS generation via tandem reactions on the BFBT nanoreactor. To gain a clearer understanding of the electronic redistribution at the Fe active sites, we further analyzed the Bader charge transfer of Fe. The results indicated that the transferred charge from the active Fe center near OV was 1.28 e in BF and 1.20 e in BFBT, suggesting an increase in charge density in BFBT (Fig. 3, G and H). However, the transferred charge from Fe sites located away from the OV increased to 1.36 e and 1.24 e, respectively (Fig. 3, I and J). This suggested that in BFBT, the electron-rich OVs donated more electrons to the Fe active sites, leading to a faster Fe(III)/Fe(II) cycle and achieving a real-time recovery of Fe(II). In conclusion, the Fe active sites of BFBT received an increased electron supply modulated by OVs, resulting in enhanced sono-piezodynamic CDT tandem reactions to produce more ROS with self-supplied H_2O_2 (Fig. 3K).

Antibacterial assessment in vitro

Titanium underwent surface pore making through alkali-heat treatment (porous Ti, T), leading to the development of well-defined porosity and a high surface area (fig. S28A) (*47*). These surfaces were further modified with pDA [Ti@pDA (Tp)], nano-HA [Tp@HA (TH)], and BFBT (TH-BFBT). We selected a concentration of 3 mg/ml of BFBT nanoparticles to optimize the loading amount and efficiency of BFBT on the scaffold (fig. S28B). SEM results indicated that the morphologies of HA, BF, and BFBT remained unchanged after being loaded onto the Ti scaffold (fig. S28, C and D). XRD analysis revealed that TH, TH-BF, and TH-BFBT exhibited diffraction peaks similar to those of HA, BF, and BFBT, respectively, indicating that loading did not alter the crystalline structure of the nanoparticles (fig. S29, A and B). In addition, TH-BFBT demonstrated excellent ROS generation capacity, reflecting piezocatalytic properties comparable to those of the nanoparticles (fig. S29, C and D). After being loaded onto the Ti scaffold, the Fe(II) content in BFBT remained stable, preserving its high catalytic reactivity. Furthermore, the Fe(II) content showed a slight increase after the reaction with H_2O_2, indicating that the loading process did not interfere with the Fe(III)/Fe(II) valence cycling and maintained a high level of Fe(II) (fig. S29, E and F). The stability of the BFBT coating on TH-BFBT under US stimulation was investigated by measuring the released BFBT using inductively coupled plasma (ICP) (fig. S30). In process 1, both released Fe ions and BFBT from the scaffolds were included, while process 2 included only the released Fe ions. The ICP analysis revealed that both processes had similar Fe concentrations, suggesting that the BFBT coating remained firmly attached to the TH-BFBT surface, likely due to the strong adhesive properties of pDA (*48*). Initially, the in vitro antibacterial efficacy of different scaffolds against *Staphylococcus aureus* (*S. aureus*) and *Escherichia coli* (*E. coli*) was examined by the spread plate method (fig. S31). Under US, TH-BFBT demonstrated remarkable bacterial viability rates of 6.9% for *S. aureus* and 5.7% for *E. coli* (Fig. 4, A and B). Its exceptional antibacterial property was derived from the explosive generation of ROS through US-driven tandem catalysis between SPT and CDT. Moreover, TH-BFBT demonstrated enhanced antibacterial performance compared to TH-BF because of superior piezoelectric properties and increased electron density on Fe of BFBT. Without US, TH-BFBT exhibited inadequate antibacterial performance without SPT. The membrane integrity and morphology of *S. aureus* and *E. coli* posttreatment were assessed by SEM (fig. S32). Notably, bacteria in Tp and TH groups showed typical spherical (*S. aureus*) or rod-shaped (*E. coli*) morphology. In TH-BF + US and TH-BFBT groups, minor surface irregularities were observed. However, the TH-BFBT + US group displayed more surface folding, shrinkage, and cracking. The antibiofilm efficacy was assessed using Live/Dead and crystal violet staining. Live/Dead results showed severe disruption and fragmentation of the bacterial biofilm with intense red fluorescence after TH-BFBT + US treatment, indicating extensive bacterial eradication (Fig. 4C). Crystal violet staining revealed a significantly reduced violet stain in TH-BFBT + US–treated biofilms, with optical density at 570 nm confirming this disruption (fig. S33). To examine bacteria microscopically, we analyzed the bio-TEM images. Bacteria treated with TH-BFBT + US exhibited incomplete cell walls and cytoplasmic leakage, whereas bacteria treated with Tp + US retained intact morphology (Fig. 4, D and E). To investigate contributing factors in the antibacterial process, we co-incubated *S. aureus* with TH-BFBT and EDTA (an iron

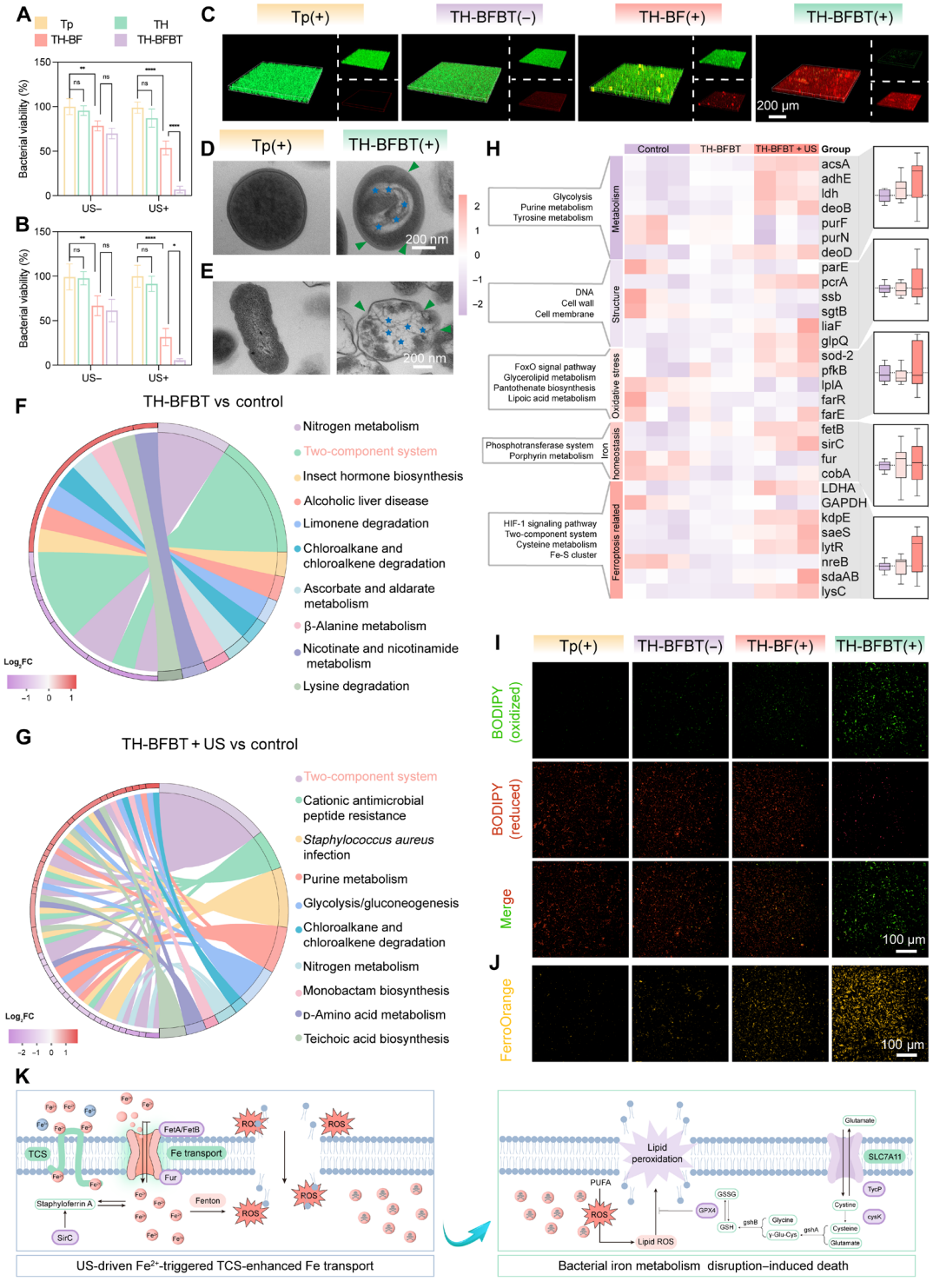

Fig. 4. Antibacterial activity of the TH-BFBT scaffold in vitro. Antibacterial results of Tp, TH, TH-BF, and TH-BFBT against (**A**) *S. aureus* and (**B**) *E. coli*. (**C**) 3D CLSM images of *S. aureus* biofilms stained with Live/Dead after incubation on various scaffolds. Bio-TEM images of (**D**) *S. aureus* and (**E**) *E. coli*. The blue pentagrams indicate sparse organelles, and the green arrows indicate plasmolysis. KEGG enrichment of top 10 relevant pathways in response to (**F**) TH-BFBT and (**G**) TH-BFBT + US. (**H**) Left: heatmap of DEGs in pathways related to metabolism, structure, oxidative stress, iron homeostasis, and ferroptosis. Right: log_2FC of DEGs in different pathways. (**I**) Lipid peroxidation induced by different treatments in *S. aureus*. (**J**) Fe(II) level in *S. aureus* with different treatments. (**K**) Schematic illustration of antibacterial mechanisms of TH-BFBT. Purple circles indicated up-regulated or down-regulated genes. [(A and B) $n = 3$ biologically independent samples; ANOVA followed by Tukey's multiple comparisons; data were presented as mean values ± SD; error bars, SD. Significant differences between groups were indicated as $^{****}P < 0.0001$, $^{**}P < 0.01$, $^{*}P < 0.05$; ns, not significant. (C to E, I, and J) A representative image of three biological replicates from each group was shown.]

chelator), which inhibited the Fe-mediated Fenton reaction, reducing •OH production and resulting in 25.3% bacterial viability because of limited ROS assault by SPT (fig. S34). In addition, bacteria co-incubated with leaching solution of TH-BFBT after 30 min of US stimulation for 24 hours showed 66.1% viability, indicating the antibacterial efficacy of the released Fe ions. The stable antibacterial property of TH-BFBT was demonstrated through a cyclic antibacterial test, simulating the continuous interaction with bacteria in a biological setting. In each cycle, TH-BF and TH-BFBT were first exposed to bacteria for 24 hours, followed by either US treatment or no treatment before seeding bacteria on culture plates, and then disinfected with ethanol. From day 1 to day 7, the antibacterial rate of TH-BFBT remained nearly constant, whereas TH-BF showed slightly lower antibacterial performance and a gradual decline over time (fig. S35).

Biological analysis of the antibacterial mechanism

To delve deeper into the intricate mechanism, we conducted RNA sequencing analysis on *S. aureus* treated with the TH-BFBT scaffold. Volcano plots depicted that 300 genes were up-regulated and 293 genes were down-regulated in TH-BFBT without US compared to the control. In addition, the TH-BFBT + US group demonstrated 349 genes up-regulated and 316 genes down-regulated (fig. S36). The correlation analysis depicted that the three groups were comparable (fig. S37). Differentially expressed genes (DEGs) underwent Gene Ontology analysis (fig. S38). Furthermore, the DEGs underwent Kyoto Encyclopedia of Genes and Genomes (KEGG) annotation analysis (fig. S39). The top 10 pathways showed that significant enrichment ($P < 0.05$) revealed significant impacts of TH-BFBT on *S. aureus*, notably in nitrogen metabolism, TCS, limonene degradation, ascorbate metabolism, and β-alanine metabolism (Fig. 4F). Nevertheless, TH-BFBT + US primarily influenced TCS, cationic antimicrobial peptide resistance, purine metabolism, glycolysis, and nitrogen metabolism (Fig. 4G). The TCS showed a notable enrichment index and low *P* value in both enrichment analyses, prompting us to further investigate bacterial ferroptosis-like death. Ferroptosis refers to a type of controlled cell death marked by iron-dependent phospholipid peroxidation (*49*). Bacterial TCSs are signal transduction systems consisting of a response regulator that adjusts gene expression to modulate the response and a cognate sensor histidine kinase that detects specific signals (*50*). Excess extracellular Fe(II) inactivated the defensive efficacy of TCS and disrupted iron homeostasis, inducing iron-induced toxicity in pathogens and lastly leading to ferroptosis (*32*). Notably, we observed both up-regulation and down-regulation of related genes in TH-BFBT and TH-BFBT + US groups, culminating in a phenomenon reminiscent of bacterial iron homeostasis and ferroptosis, with a more pronounced effect evident in the TH-BFBT + US group (Fig. 4H). To further confirm ferroptosis induced by TH-BFBT, we assessed intracellular ROS using DCFH-DA as a probe and observed higher fluorescence in the TH-BFBT + US group, indicating increased ROS levels from the Fe(II)-mediated Fenton reaction (fig. S40). Subsequently, we examined cellular lipid peroxidation using a C11 BODIPY fluorescent probe. *S. aureus* treated with TH-BFBT + US exhibited the highest level of lipid peroxidation, followed by TH-BF + US (Fig. 4I and fig. S41). Moreover, increased levels of intracellular Fe(II) accumulation were observed in *S. aureus* treated with TH-BFBT + US using the FerroOrange fluorescent probe, which is a characteristic hallmark of ferroptosis (Fig. 4J and fig. S42). In conclusion, the stability and resistance to depletion of Fe(II) reduced the defensive efficacy of TCS, resulting in disrupted bacterial iron homeostasis and increased intracellular ROS levels. The synergistic impact of disrupted TCS and elevated ROS, both intra- and extracellular, compromised the integrity of the bacterial membrane, leading to Fe(II) accumulation and further ROS production within the bacteria, ultimately inducing bacterial ferroptosis-like death. In addition, we provided a detailed illustration of the alterations in ferroptosis and the associated gene expression changes (Fig. 4K).

Osteogenesis and immunomodulation in vitro

To assess the osteogenic capability of various scaffolds, we first evaluated their cell adhesion and proliferation abilities. Cell viability assessed via Live/Dead assay and Cell Counting Kit-8 (CCK-8) revealed minimal cytotoxicity across all scaffolds (Fig. 5A and fig. S43A). We then assessed the potential cytotoxicity of US-driven piezocatalysis using the CCK-8 assay (fig. S43B). Cell viability decreased to 78.7% with TH-BF and 72.9% with TH-BFBT under US. However, cell activity recovered after 2 days of further culture, and all groups showed similar proliferation after 4 days, indicating that short-term irradiation did not cause lasting toxicity. Moreover, the TH-BFBT scaffold was fully infiltrated by cells with an elongated actin cytoskeleton, demonstrating excellent cell adhesion (fig. S43C). SEM results demonstrated consistent outcomes, with the TH-BFBT scaffold exhibiting enhanced cell spreading and tight adhesion, characterized by notably elongated filopodia (fig. S43D). As for osteogenic performance, alkaline phosphatase (ALP) expression demonstrated a notable increase within the TH-BFBT scaffold on both the 7th and 14th days, indicating enhanced cellular proliferation. On the 14th day, qualitative ALP staining revealed a distinct purple hue exclusively observed in the TH-BFBT group, suggesting the highest ALP activity (fig. S43, E and F). In addition, bone morphogenetic protein 2 (BMP-2) and Runt-related transcription factor 2 (RUNX2) were selected to assess the osteogenic capacity of TH-BFBT. The expression levels of BMP-2 and RUNX2 were greatly higher in the TH-BFBT group (Fig. 5, B to E). It has been reported that the electrical microenvironment generated by piezoelectric materials played a crucial role in osteogenesis and could facilitate macrophage polarization (*37*, *51*). To further find out the mechanism on osteogenesis, we investigated whether TH-BFBT, characterized by high spontaneous polarization, could produce an electric signal under local tissue pressure. Finite element modeling was used to calculate the piezopotential generated by BF and BFBT when subjected to mechanical stresses typically exerted by cells, which range from 0.1 to 10 nN. The analysis revealed that BFBT produced a notably higher piezopotential, ranging from 92.30 μV to 9.23 mV, compared to BF under identical mechanical forces (fig. S44). Besides, we assessed intracellular Ca^{2+} concentrations using the fluorescent probe Fluo-4 AM, which represents a mechanism underlying the promotion of osteogenesis through electrostimulation. The Ca^{2+} levels of TH-BFBT experienced a notable increase, suggesting that electrostimulation generated by BFBT led to elevation in intracellular calcium concentration (Fig. 5F and fig. S45). Furthermore, the immunomodulatory properties of TH-BFBT were investigated because of the association of M1 macrophages with inflammation and M2 macrophages in bone regeneration during infected bone loss. The immunofluorescence result and quantitative analysis demonstrated a significant reduction in inducible nitric oxide synthase (iNOS) expression (a surface marker of M1 macrophages) and a concomitant increase in cluster of differentiation 206

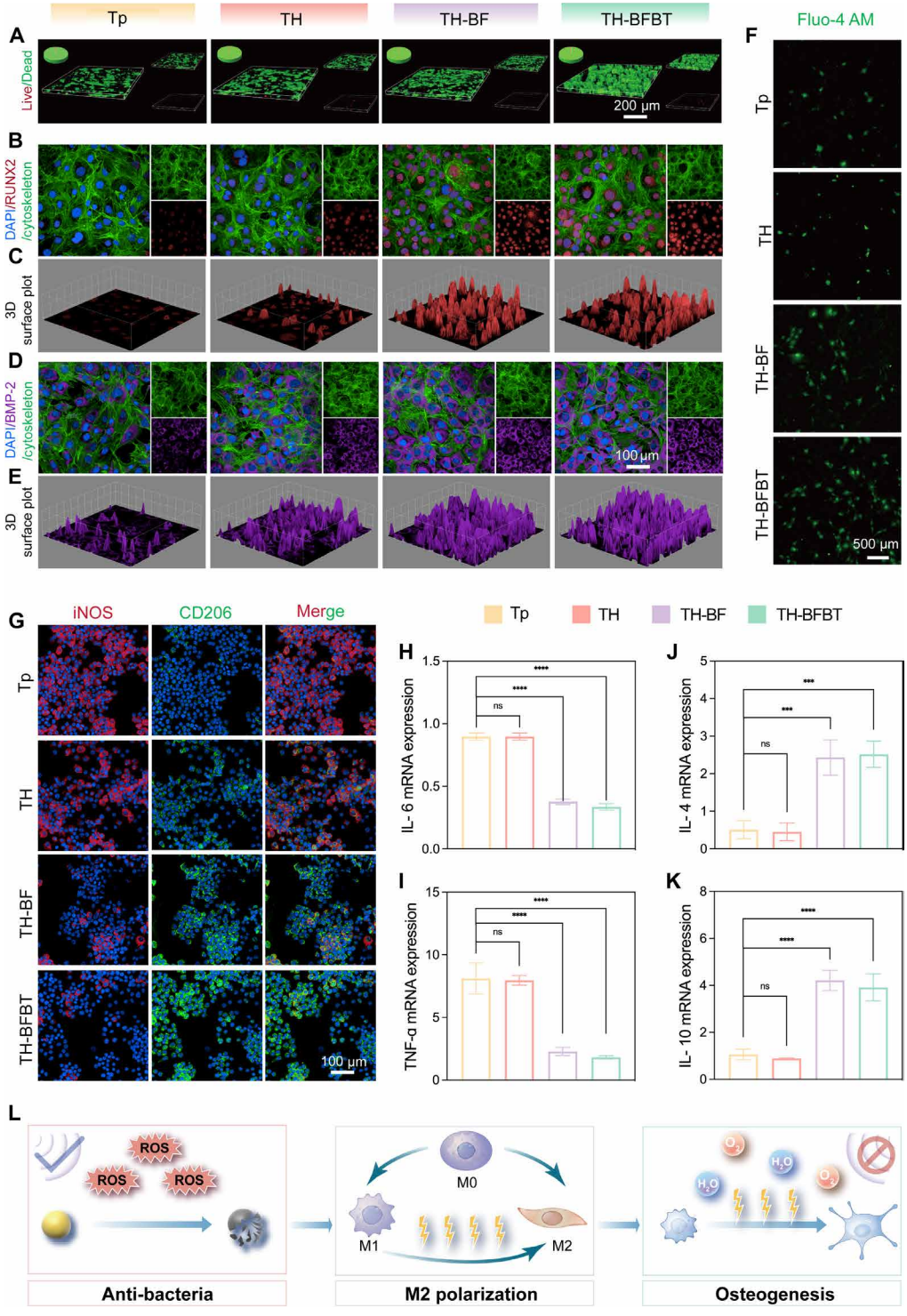

Fig. 5. In vitro evaluation of the biocompatibility, osteogeneses, and immunomodulatory properties. (**A**) MC3T3-E1 cell proliferation measured by Live/Dead assay. (**B**) Expression of RUNX2 in MC3T3-E1 cells detected via immunofluorescence and (**C**) its 3D surface plot. (**D**) Expression of BMP-2 in MC3T3-E1 cells detected via immunofluorescence and (**E**) its 3D surface plot. (**F**) Intracellular calcium level of cells detected by Fluo-4 staining. (**G**) Expression of iNOS and CD206 in RAW 264.7 macrophages detected via immunofluorescence. Relative mRNA expression levels of pro-inflammatory genes [(**H**) *IL-6* and (**I**) *TNF*-α] and anti-inflammatory genes [(**J**) *IL-4* and (**K**) *IL-10*] of macrophage. (**L**) Schematic diagram of immune regulation and bone repair by TH-BFBT. [(H to K) $n = 3$ biologically independent samples; ANOVA followed by Tukey's multiple comparisons; data were presented as mean values ± SD; error bars, SD. Significant differences between groups were indicated as ****$P < 0.0001$ and ***$P < 0.001$; ns, not significant. (A to G) A representative image of three biological replicates from each group was shown.]

(CD206) expression (a surface marker of M2 macrophages) upon treatment with TH-BFBT (Fig. 5G and fig. S46). To explore the cytokine profile, we conducted quantitative reverse transcription polymerase chain reaction experiments. The results revealed a notable decrease in the expression of pro-inflammatory cytokines [interleukin-6 (*IL-6*) and tumor necrosis factor–α (*TNF*-α)] in the TH-BFBT group (Fig. 5, H and I). Conversely, there was a significant increase in the expression of anti-inflammatory gene markers (*IL-4* and *IL-10*) in the TH-BFBT group (Fig. 5, J and K). The findings implied that the electrical microenvironment provided by TH-BFBT had the capacity to modulate immune responses, fostering polarization toward the M2 macrophage phenotype, ultimately accelerating bone repair after the pro-inflammatory antibacterial process (Fig. 5L).

Antibacterial performance in vivo

To evaluate in vivo antibacterial and osteogenic efficacy, we surgically placed scaffolds infected with *S. aureus* into bone defects of femoral condyle in Sprague-Dawley rats (Fig. 6A and fig. S47). On the seventh day postsurgery, the animals were euthanized after the treatment of 6 days with US, and their femurs were harvested for bacteriological and histological analyses. Bacterial samples collected from the scaffolds were cultured in both liquid and solid Luria-Bertani (LB) media, yielding quantitative outcomes. Both approaches confirmed that TH-BFBT(+) showed superior antibacterial efficacy compared to other groups (Fig. 6, B and C). Hematoxylin and eosin (H&E) staining showed neutrophil infiltration around the bone defect in Tp(+), TH(+), and TH-BFBT(−) groups, and fewer neutrophils were found in TH-BF(+) and the least in TH-BFBT(+) (Fig. 6, D and E). Furthermore, Giemsa staining was conducted to evaluate the infection of the injury, revealing that the TH-BFBT(+) group showed fewer bacteria (Fig. 6, F and G). To further evaluate the real-time antimicrobial efficacy in vivo, we used fluorescently labeled bacteria (DiR iodide) and implanted them into the host using the same methodology. The fluorescence intensity was then used to visualize the bacterial status. We subjected the rats to US and observed a considerable reduction in fluorescence intensity over time in the TH-BFBT(+) group, while the intensity remained relatively stable in the Tp(+) group, indicating the robust antimicrobial capability of TH-BFBT under US conditions (Fig. 6, H and I). We further assessed the ROS-generating capability of TH-BFBT in vivo over a period of 7 days. The results demonstrated that the ROS generation by TH-BFBT remained consistent when subjected to US stimulation throughout the 7-day period, highlighting its sustained antibacterial efficacy (fig. S48).

Osteogenic performance in vivo

Rat femurs were scanned using microcomputed tomography (micro-CT) at 4- and 8-week intervals postimplantation, producing detailed three-dimensional (3D) reconstructions of the femoral condyles through Imaris software. The reconstructions showed notable bone loss around defects in Tp(+) and TH(+), likely due to bacterial proliferation–induced osteolysis, while TH-BFBT(+) exhibited robust in vivo osteogenic activity with considerable new bone formation (Fig. 7A). Micro-CT quantitative analysis highlighted distinctive parameters including trabecular thickness (Tb.Th), trabecular number (Tb.N), trabecular separation (Tb.Sp), and bone volume/total volume (BV/TV), with TH-BFBT exhibiting notable differences (Fig. 7, B to E). Calcitonin and alizarin red S were intraperitoneally injected to mark the bone formation areas for assessing new bone deposition rates. The largest separation and area between the two calcium deposition lines were observed in TH-BFBT (Fig. 7F). This indicated that TH-BFBT necessitated outstanding antibacterial and osteogenic capabilities in vivo.

Histological analyses, including H&E, toluidine blue (TB), and Goldner trichrome staining, were subsequently conducted to evaluate the potential enhancement of bone formation by the piezoelectric scaffold in vivo (Fig. 8A). The H&E staining revealed evident formation of a new bone in TH-BFBT(+). TB-stained sections showed enhanced new bone growth encircling the scaffolds in TH-BFBT(+) at 8 weeks. Goldner staining revealed an increased mineralized bone of TH-BFBT(+) through its antibacterial and osteogenic capabilities. Quantitative analysis of this staining indicated that TH-BFBT(+) exhibited a greater percentage of new bone area compared to other groups (fig. S49). In the immunofluorescence examination, tissue staining revealed a notable increase in CD206-positive areas and a reduction in iNOS-positive areas treated with TH-BFBT(+) compared to other groups, highlighting its potent immunomodulatory effects in promoting M1-to-M2 macrophage polarization (Fig. 8, B to D). The assessment of blood vessel and bone ingrowth was conducted through four-color immunofluorescence using 4′,6-diamidino-2-phenylindole (DAPI), Runx2, BMP-2, and CD31 markers (Fig. 8E). The expression levels of osteogenesis-related factors, Runx2 and BMP-2, were markedly elevated in TH-BFBT(+), suggesting the capacity of implants to stimulate bone formation and fulfill the essential criteria for facilitating optimal bone growth around implants (Fig. 8, F and G). Moreover, it revealed the increased fluorescence intensity of CD31 in TH-BFBT, indicating enhanced vascularization (Fig. 8H). The heightened expression of osteogenesis-associated proteins might be ascribed to the antibacterial efficacy of TH-BFBT under the sono-piezoelectric tandem reaction combined with the ferroptosis process and the immunomodulatory ability of the piezoelectric scaffolds. Furthermore, histological assessment of dissected organs demonstrated the absence of structural changes, suggestive of commendable biosafety (fig. S50). Hematological profiling additionally unveiled favorable indicators within the experimental cohort (fig. S51), thereby affirming the commendable biocompatibility and limited adverse reactions of TH-BFBT.

DISCUSSION

Current clinical strategies for managing IAIs primarily involve antibiotics and the physical removal of infected tissues or implants. However, repeated antibiotic use increases the risk of drug resistance, and biofilm formation often limits drug penetration. Severe pain and disability have been documented when IAIs become difficult to reverse. We believe that an antibiotic-free, ROS-enabled bacterial dynamic therapy, recognized as a noninvasive treatment, can effectively alleviate IAIs. Lead-free piezoelectric nanocrystals used as sonosensitizers have also been explored to address bacterial infections. In this design, we incorporate a multifunctional defect-rich nanoreactor into the Ti scaffold, providing superior antibacterial efficacy through sono-piezoelectric tandem catalysis while also enhancing bone regeneration by modulating macrophage responses.

In conclusion, we developed a US-triggered piezoelectric nanoreactor for the effective treatment of IAIs. Upon US stimulation, BFBT initiates the tandem catalysis of SPT and CDT, where self-supplied H_2O_2 from SPT serves as the reaction substrate for CDT,

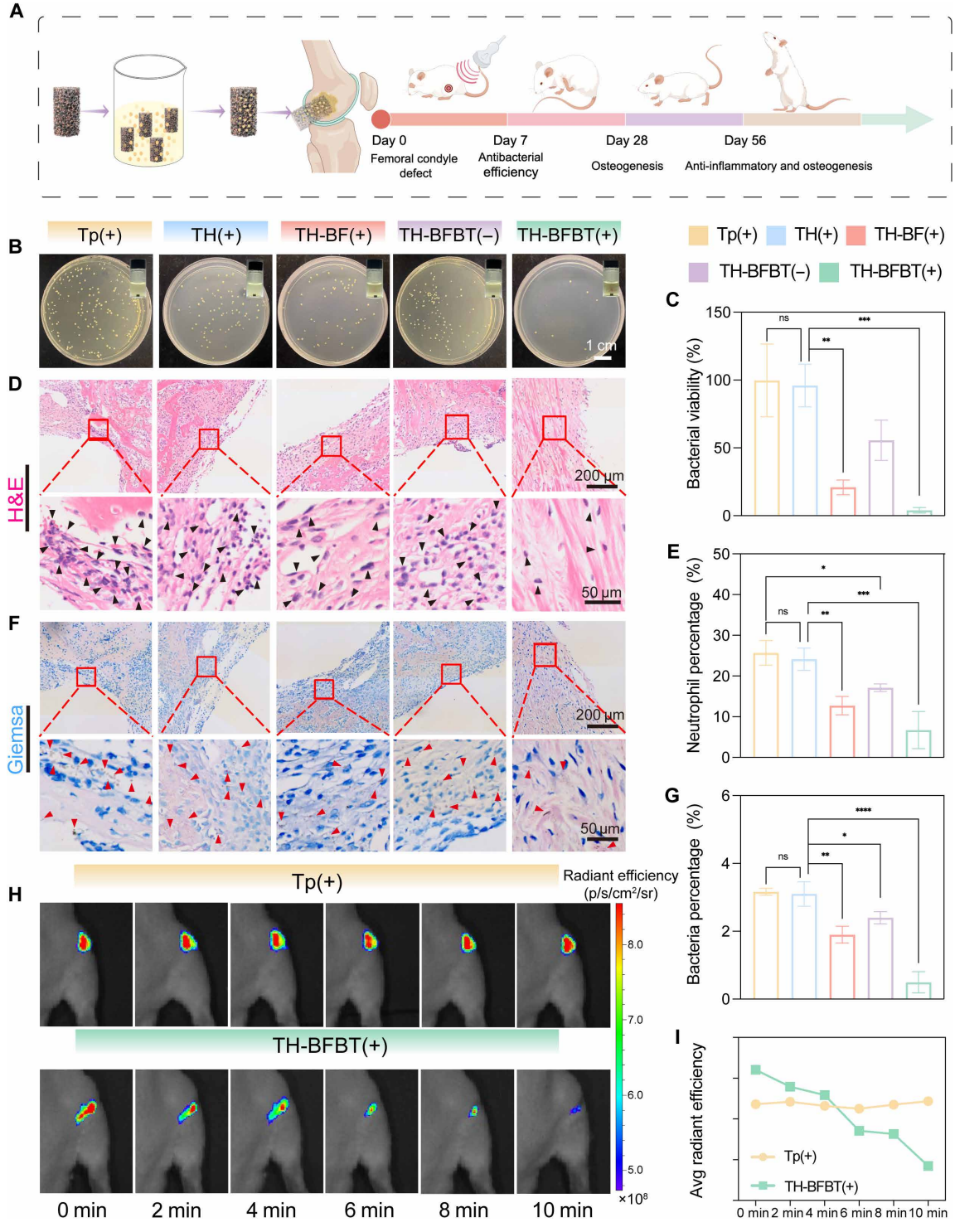

Fig. 6. Antibacterial activity of the TH-BFBT scaffold in vivo. (**A**) Schematic illustration of infected modified Ti scaffolds and animal experimental treatment in therapeutics. (**B**) Images of bacterial colonies and turbid liquid of different groups. (**C**) Quantitative analysis of antibacterial efficiency based on CFUs after different treatments. (**D**) H&E images and (**E**) semiquantification of neutrophils in the infected bone tissues surrounding the implants. The arrows represented neutrophils. (**F**) Giemsa staining images and (**G**) semiquantification of bacteria in the infected bone tissues surrounding the implants. The arrows represented bacteria. (**H**) IVIS images and (**I**) changes in fluorescence intensity of Tp(+) and TH-BFBT(+). [(C, E, and G) $n = 3$ biologically independent samples; ANOVA followed by Tukey's multiple comparisons; data were presented as mean values ± SD; error bars, SD. Significant differences between groups were indicated as $^{****}P < 0.0001$, $^{***}P < 0.001$, $^{**}P < 0.01$, and $^{*}P < 0.05$; ns, not significant. (B, D, and F) A representative image of three biological replicates from each group was shown.]

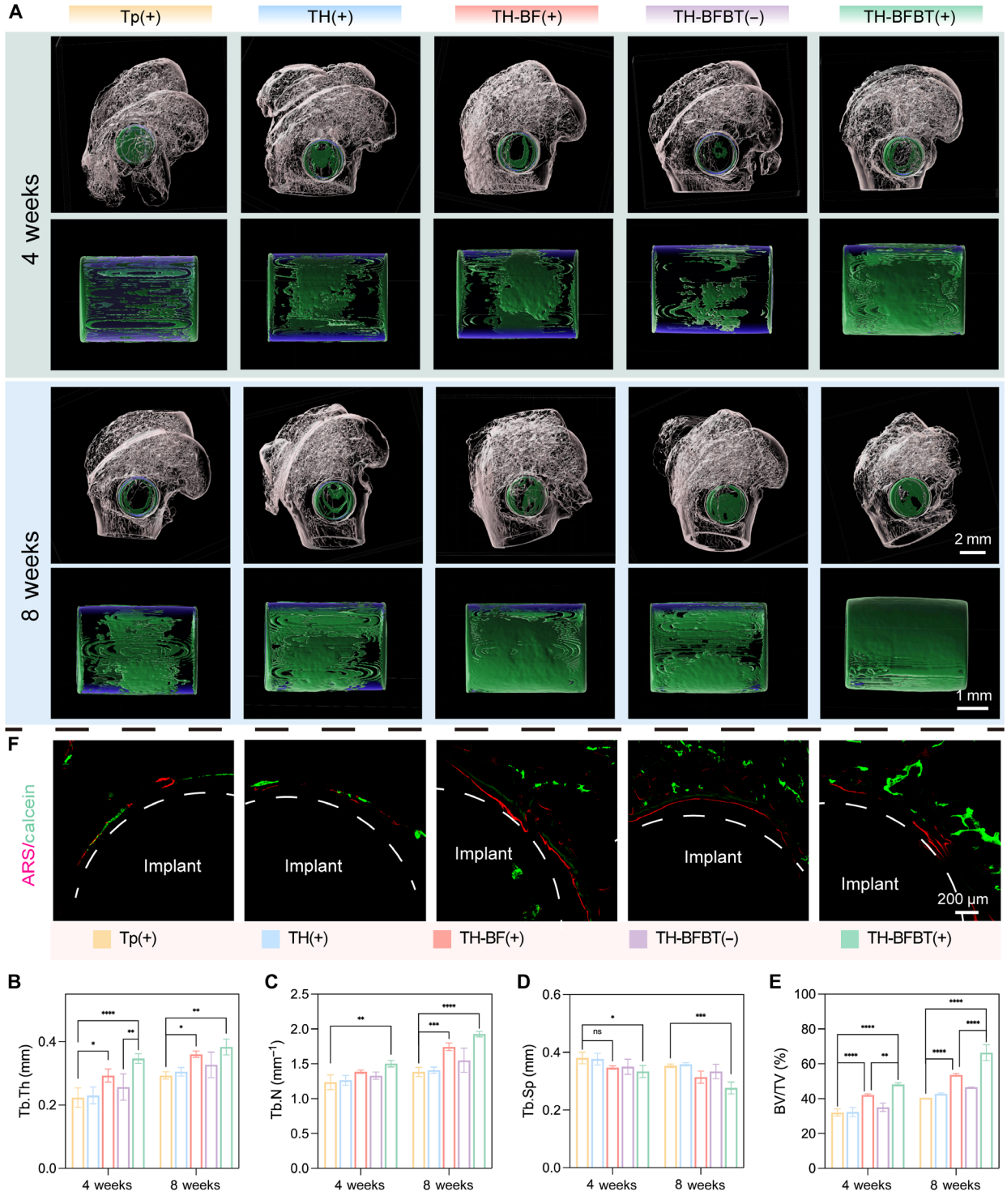

Fig. 7. Bone regeneration in vivo. (**A**) Micro-CT of femoral condyle. Top: reconstruction of the defect and new bone ingrowth around the scaffolds. Bottom: side view of new bone with the scaffolds. Quantitative statistics of the bone regeneration–related index in 3D reconstruction by micro-CT including (**B**) Tb.Th, (**C**) Tb.N, (**D**) Tb.Sp, and (**E**) BV/TV. (**F**) Calcitonin (green)– and alizarin red S (red)–marked new bone. [(B to E) $n = 3$ biologically independent samples; ANOVA followed by Tukey's multiple comparisons; data were presented as mean values ± SD; error bars, SD. Significant differences between groups were indicated as ****$P < 0.0001$, ***$P < 0.001$, **$P < 0.01$, and *$P < 0.05$; ns, not significant. (A and F) A representative image of three biological replicates from each group was shown.]

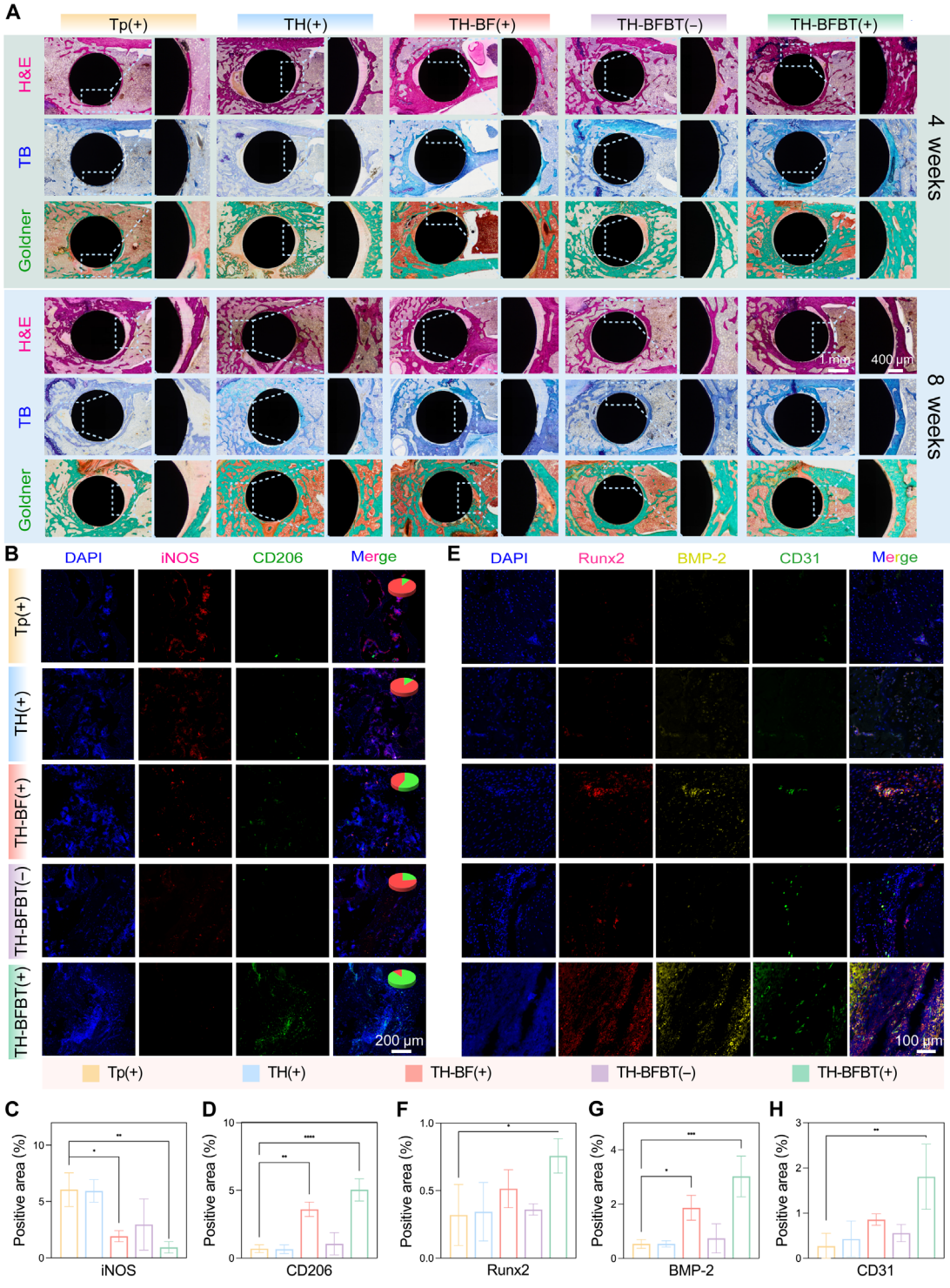

Fig. 8. Histological and immunofluorescence analyses. (**A**) H&E, TB, and Goldner staining of undecalcified tissue around the implant at 4 (first row) and 8 (second row) weeks postsurgery. Immunofluorescence staining of (**B**) iNOS and CD206 and (**E**) Runx2, BMP-2, and CD31 surrounding tissues of implants at 8 weeks postsurgery. Quantification of (**C**) iNOS, (**D**) CD206, (**F**) Runx2, (**G**) BMP-2, and (**H**) CD31 immunoreactivity around the implants. [(C, D, and F to H) $n = 3$ biologically independent samples; ANOVA followed by Tukey's multiple comparisons; data were presented as mean values ± SD; error bars, SD. Significant differences between groups were indicated as $^{****}P < 0.0001$, $^{***}P < 0.001$, $^{**}P < 0.01$, and $^{*}P < 0.05$; ns, not significant. (A, B, and E) A representative image of three biological replicates from each group was shown.]

leading to notably enhanced ROS production. In addition, the efficacy of CDT is also contingent upon the ability of OVs to regulate the local electronic structure, facilitating the reduction of Fe(III) and accelerating Fe(III)/Fe(II) redox cycles, thereby sustaining a self-cycled Fenton reaction. Transcriptomics analysis revealed that sustained Fe(II) levels disrupt the TCS of *S. aureus*, leading to dysregulation of bacterial iron metabolism and ultimately triggering ferroptosis-like death. In addition to its bactericidal effects, BFBT facilitates osteogenesis in the postantibacterial phase. The reduction in M1 macrophage markers and the increase in M2 markers suggest that the nanoreactor effectively modulates the postantibacterial inflammatory environment, thereby promoting bone repair through the electric signals generated by BFBT. In vivo experiments demonstrated that TH-BFBT, after US stimulation, significantly enhanced new bone formation in Sprague-Dawley rats with IAIs, attributable to the multifunctional effects of the nanoreactor, including ROS-mediated antibacterial activity, bacterial ferroptosis-like death, and immunomodulation-driven osteogenesis. Our research provides a potential strategy for designing lead-free piezoelectric materials in the biomedical field, with potential applications not only in the efficient treatment of IAIs but also in combating other infections.

MATERIALS AND METHODS

Chemicals

Nano-HA, Bi_2O_3 (99%), Fe_2O_3 (98%), $BaCO_3$ (99%), and TiO_2(98%) were bought from Sinopharm Chemical Reagent Co., Ltd. (China). Commercial titanium implants were obtained from Baoji Shengzen Metal Co., Ltd. (China). Dopamine hydrochloride, MB, alizarin red S, and calcein were obtained from Sigma Chemical Co. DPBF was from Aladdin (China).

Synthesis of BFBT nanocrystals

BF and BFBT were constructed by the solid-state reaction method. The alcohol and ZrO_2 balls were mixed with Bi_2O_3 (99%, 21.18 g), Fe_2O_3 (98%, 7.33 g), $BaCO_3$ (99%, 1.99 g), and TiO_2 (98%, 0.82 g) in nylon jars for ball-milling (120 rpm, 24 hours). The mixture was then calcined at 850°C for 6 hours, followed by sand grinding at 2000 rpm for 8 hours (VB-0.3Q, Suzhou Vgreen Nano-chem Technology Co., Ltd., China).

Preparation of the TH-BFBT scaffold

The titanium scaffold was agitated in a 10 mM tris-HCl buffer (pH 8.5) including dopamine hydrochloride (3 mg/ml) for 24 hours, leading to the formation of Tp. Subsequently, the Tp scaffold was submerged in an HA solution (3 mg/ml) for 12 hours to create TH. The TH-BF and TH-BFBT scaffolds were then developed by soaking the TH scaffolds in varying solutions (3 mg/ml) for 18 hours.

Characteristics

XRD (Rigaku Ultima IV, Cu Kα radiation) was applied to measure the structures of samples. Raman spectra were obtained using Raman spectroscopy with a 532-nm excitation wavelength (Invia Reflex, Renishaw, UK). EPR (A300, Bruker, Germany) was conducted to probe C_{OV}. XPS (K-Alpha+, Thermo Fisher Scientific, United States) was applied to test the chemical state. The ferroelectric characteristic was identified through SHG analysis using the MStarter 100 SHG Microspectral Scanning Test System (Nanjing Metatest Optoelectronics Co., Ltd., China). Electrochemical experiments were conducted applying a three-electrode system on an electrochemical workstation (CHI660E, Shanghai Chenhua Instrument Corporation, China) to measure the piezocurrent, charge transfer resistance, and flat band potential through Mott-Schottky and Nyquist plots. The working electrode was F-doped SnO_2 glass coated with a piezoelectric catalyst, the reference electrode was a Ag-AgCl electrode, and the counter electrode was platinum. A Na_2SO_4 (0.1 M) solution served as the supporting electrolyte, and mechanical vibration was applied using a variable power ultrasonic machine (40 kHz). The surface morphologies were examined using SEM (Gemini 300, ZEISS, Germany). Using HR-TEM (JEM-F200, JEOL, Japan), the related lattice fringes and high-resolution images were captured. The release of Fe ions from TH-BFBT scaffolds was measured using an ICP–mass spectrometry spectrometer (7850, Agilent, United States). For this analysis, the scaffolds were immersed in a 0.9% NaCl solution at 37 ± 1°C, following the international standard ISO 10993-12, with a surface-area-to-volume ratio of 3 cm^2/ml. Triplicate samples were used to obtain the average value along with the SD.

Iron concentration

The concentration of Fe(II) was determined using 1,10-phenanthroline spectrophotometry. The Fenton degradation reaction solution (1 ml) was filtered and combined with acetic acid/sodium acetate solution (2 ml, Macklin, China) and 0.4 ml of 1,10-phenanthroline (Macklin, China) solution (1.2 g $liter^{-1}$) in a colorimetric tube. The solution was adjusted to 10 ml, and then after 5 min of color development, a UV-vis spectrophotometer (UV-5200, METASH, China) served to get the absorbance at 510 nm.

In vitro detection of ROS

The ROS produced upon exposure to US stimulation were assessed using MB, DPBF, Rhodamine B (RhB), potassium permanganate, and EPR techniques. To evaluate the production of •OH, various materials were combined with MB and exposed to US (1.5 W/cm^2, 1 MHz, 50% duty cycle) with or without H_2O_2 (0.5 mM). The alterations in MB (Macklin, China) absorption at 664 nm before and after US stimulation were measured by a UV-vis spectrophotometer (UV-5200, METASH, China). Similarly, DPBF exhibits specific oxidation by $•O_2^-$, evident through a reduction in the absorption peak at 410 nm. Active species trapping experiments were performed to determine the key active species involved in US-induced piezoelectric degradation. RhB was selected as the probe dye for this study. The absorbance of RhB at 554 nm was monitored to assess the degradation effect in the presence of different scavengers. To verify the self-supplying capability of H_2O_2 by BFBT, a potassium permanganate–based colorimetric assay was used to measure the formation of H_2O_2, which is indicated by an enhancement in absorbance at 525 nm. DMPO (5,5-dimethyl-1-pyrroline-*N*-oxide) (0.1 mM) was used to detect •OH by an EPR spectrometer (A300, Bruker, Germany).

Theoretical calculations of the electronic structure of BF and BFBT

DFT calculations were conducted using the projector augmented wave method within the Vienna Ab Initio Simulation Package (*52*). The exchange-correlation potential was chosen according to the generalized gradient approximation by Perdew, Burke, and Ernzerhof (*53*). Van der Waals interactions, especially long-range ones, were accounted for via the DFT-D3 methodology (*54*). Plane wave cutoff energy was fixed at 500 eV, with the iterative Kohn-Sham

equation solution's energy threshold set at 10^{-6} eV. To mitigate spurious interactions between periodic images, a 15-Å vacuum layer was introduced perpendicular to the sheet. The K-mesh was refined in real space with a resolution of 0.04 2π/Å. Structural relaxations were pursued until atomic residual forces dropped below 0.05 eV/Å. In addition, a *U* parameter of 4 eV was applied to the Fe d-orbitals in BF to account for on-site Coulomb interactions between d states, following the DFT + *U* formalism.

Antibacterial assessment in vitro

S. aureus [Gram-positive, American Type Culture Collection (ATCC) 25923] and *E. coli* (Gram-negative, ATCC 25922) were cultured in sterile LB medium. Both bacteria were tested at an initial concentration of 10^4 colony-forming units (CFUs)/ml in the antimicrobial measurement. The antibacterial efficacy of Tp, TH, TH-BF, and TH-BFBT was evaluated using the spread plate method. The materials were incubated with bacterial suspensions in EP tubes. They were either subjected to US (1.5 W/cm^2, 1 MHz, 50% duty cycle) for 5 min or kept untreated. Next, 50 μl of the bacterial solution was taken and evenly spread on LB agar plates. Once the bacterial colonies reached an appropriate size, they were counted after capturing images. The same method and procedure were used for the inhibition assay of EDTA. The antibacterial efficiency of each sample was calculated using the following equation

$$\text{Bacterial viability (\%)} = \frac{\text{CFU}_{\text{Sample}}}{\text{CFU}_{\text{control}}} \times 100$$

The bacterial morphology was examined using SEM (Gemini 300, ZEISS, Germany). A diluted *S. aureus* and *E. coli* solution was added to different scaffolds for 8 hours. The US groups were then exposed to US for 5 min (1.5 W/cm^2, 1 MHz, 50% duty cycle). After incubation, the scaffolds were fixed in 4% formaldehyde for 2 hours and washed with phosphate-buffered saline (pH 7.0). The bacteria were then dehydrated with ethanol solutions, followed by gold coating before SEM observation. TEM (JEM-1400FLASH, JEOL, Japan) images were subsequently taken. Following 4 days of bacterial growth on different scaffolds to form a biofilm, the Live/Dead Bac Light viability kit (Thermo Fisher Scientific, United States) was used to perform a Live/Dead staining assay, and the data were acquired using confocal laser scanning microscopy (CLSM; N-SIM S, Nikon, Japan). Similarly, biofilms were stained with crystal violet (Biosharp, China) and images were scanned for qualitative assessment. To quantify the dye deposited on the biofilms, ethanol was used for dissolution, and the optical density was examined at 570 nm.

RNA sequencing

S. aureus (ATCC 25923) was cultured with TH-BFBT with and without US stimulation. During the logarithmic phase, the bacteria were harvested by cryocentrifugation and promptly frozen in liquid nitrogen. This experiment was replicated three times for all groups: control group (Control-1, Control-2, and Control-3), experimental group 1 (TH-BFBT-1, TH-BFBT-2, and TH-BFBT-3), and experimental group 2 (TH-BFBT + US-1, TH-BFBT + US-2, and TH-BFBT + US-3). Total RNA isolation and cDNA library construction were executed, followed by sequencing on an Illumina HiSeq platform at Majorbio Biopharm Technology Co., Ltd. DESeq2 (version 1.24.0) software was used to analyze expression quantification data, with DEGs identified using a screening threshold of $|\log_2\text{FC}$ (fold change)$| \geq 1$ and $P < 0.05$. The biological functions and pathways related to these DEGs were investigated using the KEGG (www.genome.jp/kegg/) database. KEGG pathway analysis was performed using KOBAS software, with pathway significance evaluated through Fisher's exact test, offering insights into functional differences between the samples. The heatmap was created through the online platform available at www.bioinformatics.com.cn.

Ferroptosis evaluation

Intracellular ROS levels, intracellular lipid hydroperoxides, and Fe(II) were detected using DCFH-DA (Yuanye Bio-Technology Co., China), C11 BODIPY 581/591 (Amgicam, China), and FerroOrange (Dojinto, Japan), respectively. The fluorescence intensity and images were obtained using Opera Phenix Plus (PerkinElmer, United States).

Cell proliferation and spreading assay

Mouse osteoblastic MC3T3-E1 cells (GNM15) and macrophage RAW 264.7 cells were bought from the Cell Bank of the Chinese Academy of Sciences (Shanghai, China). The cell cultures were incubated at 37°C in a humidified environment with 5% CO_2 under standard laboratory conditions for in vitro studies. The CCK-8 assay was conducted to detect cell viability using a CCK-8 kit (Beyotime, China). The microplate reader (Multiskan SkyHigh, Thermo Fisher Scientific, United States) was used to measure the absorbance on days 1, 3, and 5. In addition, cell viability was evaluated by seeding cells onto various scaffolds for 3 days and assessing them using Cytotoxicity Assay Kit/Calcein/PI Cell Viability (Beyotime, China) and observed using CLSM. MC3T3 cells were cultured on various samples for 2 days in a 12-well plate. After fixing with 4% paraformaldehyde for 2 hours and permeabilizing with 0.1% Triton X-100 for 30 min, the cytoskeleton and nucleus were stained with phalloidin and DAPI (Solarbio, China), respectively, and fluorescence imaging was performed via CLSM. Similarly, for morphological analysis, the cells were fixed for 2 hours in 500 μl of 2.5% glutaraldehyde solution and dehydrated using a series of ethanol concentrations. Following drying, the samples were examined using SEM.

Osteogenic differentiation in vitro

Following the seeding of MC3T3-E1 cells onto different scaffolds, the medium was changed to an osteoinductive medium comprising ascorbic acid (50 μg/ml), 10 nM dexamethasone, and 10 mM β-glycerophosphate (Sigma-Aldrich, United States) to promote osteogenic differentiation. The medium was changed every 3 days. ALP activity was measured on days 7 and 14 using a BCIP/NBT ALP colorimetric assay kit (Beyotime, China). Similarly, intracellular ALP levels were quantified using an Alkaline Phosphatase Assay Kit (Beyotime, China) after MC3T3-E1 cells were cultured on the scaffolds for 7 and 14 days. For the immunofluorescence analysis of BMP-2 and RUNX2, cells were incubated with specific primary antibodies: rabbit anti-BMP2 (1:200, Abcam, United States) and rabbit anti-RUNX2 (1:200, Abcam, United States). The secondary antibody used was a donkey anti-rabbit Alexa Fluor 594 antibody (1:500, Invitrogen, United States). Cells were counterstained for the cytoskeleton with fluorescein isothiocyanate–labeled phalloidin (Solarbio, China) and for nuclei with DAPI. The fluorescence intensity and images was obtained using Opera Phenix Plus (PerkinElmer, United States). In addition, the intracellular Ca^{2+} concentration was evaluated by seeding cells onto various scaffolds for 3 days and assessing

them using a Fluo-4 Calcium Assay Kit (Beyotime, China). The results were then observed using CLSM.

Immunomodulation in vitro

RAW 264.7 cells were cultured with lipopolysaccharide (10 μg/ml; L4391, Sigma-Aldrich, United States) to evaluate macrophage polarization and cultured with different groups for 24 hours. For immunofluorescence staining, cells were stained with primary antibodies to detect iNOS and CD206. The primary antibodies used were rabbit anti-CD206 (1:200, Abcam, United States) and rat anti-iNOS (1:200, Abcam, United States). Secondary antibodies included donkey anti-rabbit Alexa Fluor 594 (1:500, Invitrogen, United States) and donkey anti-rat Alexa Fluor 488 (1:500, Invitrogen, United States). After staining, cell nuclei were labeled with DAPI. The fluorescence intensity and images was obtained using Opera Phenix Plus (PerkinElmer, United States). Gene expression levels of pro-inflammatory factors (*TNF*-α and *IL-6*) and anti-inflammatory factors (*IL-4* and *IL-10*) (TsingKe Biotech Co., Ltd., Beijing, China), were measured by quantitative reverse transcription polymerase chain reaction. The housekeeping gene selected was glyceraldehyde-3-phosphate dehydrogenase, and the primer sequences are provided in table S1.

In vivo experiments

Male Sprague-Dawley rats weighing 200 to 220 g and ~2 months old of age were purchased from Beijing Huafukang Bioscience Co., Ltd. Animal studies were carried out following the ethical regulations of the Laboratory Animal Ethics Committee at West China Hospital, Sichuan University, Chengdu, China (20240313011). In the 2 weeks preceding the experiments, all rats were housed under controlled conditions, including a temperature of 25 ± 3°C, humidity of 60 to 70%, and a 12-hour light/dark cycle. Sprague-Dawley rats ($n = 9$ per group) were randomly divided to five groups: Tp(+), TH(+), TH-BF(+), TH-BFBT(−), and TH-BFBT(+). To establish an implant-related infection model, engineered Ti implants (4 mm in height and 3 mm in diameter) were submerged in a solution containing *S. aureus* (2×10^7 CFUs ml^{-1}) at 37°C for 12 hours. Following this, rats were anesthetized with 1.5% isoflurane, and a bone defect was surgically made in the lateral femoral condyle. Rats were euthanized at 1, 4, and 8 weeks postimplantation to evaluate both the antibacterial and osteogenesis efficacy.

Antibacterial efficacy in vivo

Rats underwent 5 min of US stimulation (1.5 W cm^{-2},1 MHz, 50% duty cycle) from the first day to the sixth day following surgery. The rats were euthanized, and the implants were extracted and collected in sample collection tubes for bacterial collection on the seventh day postsurgery. Agar plating of serial dilutions was performed to assess implant infection. In addition, surrounding bone tissue was collected, decalcified, and analyzed histologically using H&E and Giemsa staining to evaluate antibacterial and anti-inflammatory effects. These tissue sections were captured using Vectra Polaris (PerkinElmer, United States). To further investigate the real-time antibacterial effect in vivo, we labeled bacteria with DiR iodide (Yeasenbiotech, China) and then implanted the scaffolds into rats using the same method. Four hours later, the Tp(+) and TH-BFBT(+) groups underwent 10 min of US stimulation, and bacterial in vivo imaging was performed using the IVIS Spectrum (PerkinElmer, United States). Then, we conducted in vivo experiments to assess the ROS generation. TH-BFBT was implanted subcutaneously, and US was applied at designated intervals (or left untreated). Luminol, injected before treatment, served as the ROS indicator, with IVIS used for detection and quantification.

Osteogenesis in vivo

To evaluate osseointegration at the bone-implant interface and the thickness of the surrounding trabeculae, femoral condyles underwent scanning using the Quantum GX Micro CT (PerkinElmer, United States). CT scans were reconstructed into 3D images using Imaris 9.9 software (BitPlane, Oxford Instruments). Subsequently, Skyscan NRecon software was used to quantify parameters including Tb.Th, Tb.N, Tb.Sp, and % BV/TV. To evaluate the rate of new bone growth, rats were intraperitoneally injected with alizarin red S (30 mg kg^{-1}) and calcein (20 mg kg^{-1}) at 4 and 6 weeks after surgery. The rats were euthanized 8 weeks postimplantation. The implants, along with the surrounding bone, were then collected, sectioned, and analyzed using CLSM (Nikon, Japan).

Microstructural analysis of a new bone: Histology and immunohistochemistry

Histological sections were prepared perpendicular to the implants' longitudinal axis within the femoral condyle before decalcification. The sections were ground to a thickness of 100 μm, followed by polishing of the slides and staining with H&E, TB, and Masson's trichrome. Subsequently, the staining was performed and visualized using VS200 (Olympus, Japan). Furthermore, additional bone samples without implants underwent fixation, decalcification, dehydration, and embedding in paraffin. The tissues were sectioned and prepared for four-color immunofluorescence staining with the primary antibodies (Abcam, UK): RUNX2 (1:200, ab236639), BMP-2 (1:200, ab214821), CD31 (1:500, ab182981), and DAPI (1:1000, ab285390). In addition, three-color immunofluorescence staining was conducted using iNOS (1:1000, ab283655), CD206 (1:200, CST no. 24595), and DAPI (1:1000, ab285390). Last, four-color and three-color immunofluorescence staining was visualized using Vectra Polaris (PerkinElmer, United States).

Statistical analysis

Means ± SD were used to express the data, with error bars representing the SD. Statistical analysis involved the analysis of variance (ANOVA), followed by Tukey's multiple comparison test. Significance was marked by $*P < 0.05$, $**P < 0.01$, $***P < 0.001$, and $****P < 0.0001$.

Supplementary Materials

This PDF file includes:

Figs. S1 to S51

Table S1

REFERENCES AND NOTES

1. M. Kaur, K. Singh, Review on titanium and titanium based alloys as biomaterials for orthopaedic applications. *Mater. Sci. Eng. C* **102**, 844–862 (2019).
2. S. Li, Y. Yue, W. Wang, M. Han, X. Wan, Q. Li, X. Chen, J. Cao, Y. Zhang, J. Li, J. Li, L. Cheng, J. Yang, D. Wang, Z. Zhou, Ultrasound-activated probiotics vesicles coating for titanium implant infections through bacterial cuproptosis-like death and immunoregulation. *Adv. Mater.* **36**, 2405953 (2024).
3. W. Zimmerli, Clinical presentation and treatment of orthopaedic implant-associated infection. *J. Intern. Med.* **276**, 111–119 (2014).
4. C. R. Arciola, D. Campoccia, L. Montanaro, Implant infections: Adhesion, biofilm formation and immune evasion. *Nat. Rev. Microbiol.* **16**, 397–409 (2018).

5. M. Xie, M. Gao, Y. Yun, M. Malmsten, V. M. Rotello, R. Zboril, O. Akhavan, A. Kraskouski, J. Amalraj, X. Cai, J. Lu, H. Zheng, R. Li, Antibacterial nanomaterials: Mechanisms, impacts on antimicrobial resistance and design principles. *Angew. Chem. Int. Ed.* **62**, e202217345 (2023).
6. A. H. Holmes, L. S. P. Moore, A. Sundsfjord, M. Steinbakk, S. Regmi, A. Karkey, P. J. Guerin, L. J. V. Piddock, Understanding the mechanisms and drivers of antimicrobial resistance. *The Lancet* **387**, 176–187 (2016).
7. W. Zhou, X. Peng, Y. Ma, Y. Hu, Y. Wu, F. Lan, M. D. Weir, M. Li, B. Ren, T. W. Oates, H. H. K. Xu, X. Zhou, L. Cheng, Two-staged time-dependent materials for the prevention of implant-related infections. *Acta Biomater.* **101**, 128–140 (2020).
8. Z. Su, D. Xu, X. Hu, W. Zhu, L. Kong, Z. Qian, J. Mei, R. Ma, X. Shang, W. Fan, C. Zhu, Biodegradable oxygen-evolving metalloantibiotics for spatiotemporal sono-metalloimmunotherapy against orthopaedic biofilm infections. *Nat. Commun.* **15**, 8058 (2024).
9. L. Qin, S. Yang, C. Zhao, J. Yang, F. Li, Z. Xu, Y. Yang, H. Zhou, K. Li, C. Xiong, W. Huang, N. Hu, X. Hu, Prospects and challenges for the application of tissue engineering technologies in the treatment of bone infections. *Bone Res.* **12**, 28 (2024).
10. R. O. Darouiche, Treatment of infections associated with surgical implants. *N. Engl. J. Med.* **350**, 1422–1429 (2004).
11. J. Huo, Q. Jia, H. Huang, J. Zhang, P. Li, X. Dong, W. Huang, Emerging photothermal-derived multimodal synergistic therapy in combating bacterial infections. *Chem. Soc. Rev.* **50**, 8762–8789 (2021).
12. C. Geng, S. He, S. Yu, H. M. Johnson, H. Shi, Y. Chen, Y. K. Chan, W. He, M. Qin, X. Li, Y. Deng, Achieving clearance of drug-resistant bacterial infection and rapid cutaneous wound regeneration using an ROS-balancing-engineered heterojunction. *Adv. Mater.* **36**, e2310599 (2024).
13. Q. Wang, Y. Tian, M. Yao, J. Fu, L. Wang, Y. Zhu, Bimetallic organic frameworks of high piezovoltage for sono-piezo dynamic therapy. *Adv. Mater.* **35**, e2301784 (2023).
14. X. Wang, N. Wang, J. Liao, X. Wang, A. Zou, Q. Chen, C.-B.-W. Li, J. Zhang, D. Wang, Y. Peng, X. Lv, J. Wu, Lead-free (K, Na)NbO_3 piezocatalyst with superior piezocatalysis and large-scale production. *Adv. Funct. Mater.* **34**, 2313662 (2024).
15. S. Chen, P. Zhu, L. Mao, W. Wu, H. Lin, D. Xu, X. Lu, J. Shi, Piezocatalytic medicine: An emerging frontier using piezoelectric materials for biomedical applications. *Adv. Mater.* **35**, e2208256 (2023).
16. D.-M. Liu, J.-T. Zhang, C.-C. Jin, B.-B. Chen, J. Hu, R. Zhu, F. Wang, Insight into oxygen-vacancy regulation on piezocatalytic activity of $(Bi_{1/2}Na_{1/2})TiO_3$ crystallites: Experiments and first-principles calculations. *Nano Energy* **95**, 106975 (2022).
17. Z. Liang, C.-F. Yan, S. Rtimi, J. Bandara, Piezoelectric materials for catalytic/photocatalytic removal of pollutants: Recent advances and outlook. *Appl. Catal. B Environ.* **241**, 256–269 (2019).
18. H. Zhang, Y. Chen, W. Hua, W. Gu, H. Zhuang, H. Li, X. Jiang, Y. Mao, Y. Liu, D. Jin, W. Bu, Heterostructures with built-in electric fields for long-lasting chemodynamic therapy. *Angew. Chem. Int. Ed. Engl.* **135**, e202300356 (2023).
19. P. Zhao, H. Li, W. Bu, A forward vision for chemodynamic therapy: Issues and opportunities. *Angew. Chem. Int. Ed. Engl.* **135**, e202210415 (2023).
20. D. Jana, Y. Zhao, Strategies for enhancing cancer chemodynamic therapy performance. *Exploration* **2**, 20210238 (2022).
21. P. Zhao, Y. Jiang, Z. Tang, Y. Li, B. Sun, Y. Wu, J. Wu, Y. Liu, W. Bu, Constructing electron levers in perovskite nanocrystals to regulate the local electron density for intensive chemodynamic therapy. *Angew. Chem. Int. Ed. Engl.* **60**, 8905–8912 (2021).
22. J. Xu, Q. Zhang, X. Gao, P. Wang, H. Che, C. Tang, Y. Ao, Highly efficient Fe^{III}-initiated self-cycled Fenton system in piezo-catalytic process for organic pollutants degradation. *Angew. Chem. Int. Ed. Engl.* **62**, e202307018 (2023).
23. Y. Wu, W. Xu, L. Jiao, Y. Tang, Y. Chen, W. Gu, C. Zhu, Defect engineering in nanozymes. *Mater. Today* **52**, 327–347 (2022).
24. W. Yang, F. Qi, W. An, H. Yu, S. Liu, P. Ma, R. Chen, S. Liu, L.-L. Lou, K. Yu, Local electronic structure modulation of interfacial oxygen vacancies promotes the oxygen activation capacity of $Pt/Ce_{1-x}M_xO_{2-\delta}$. *ACS Catal.* **14**, 5936–5948 (2024).
25. J. M. Wu, Y.-G. Sun, W.-E. Chang, J.-T. Lee, Piezoelectricity induced water splitting and formation of hydroxyl radical from active edge sites of MoS_2 nanoflowers. *Nano Energy* **46**, 372–382 (2018).
26. C. Bao, H. Wang, C. Wang, X. Zhang, X. Zhao, C.-L. Dong, Y.-C. Huang, S. Chen, P. Guo, X. She, Y. Sun, D. Yang, Cooperation of oxygen vacancy and Fe^{III}/Fe^{II} sites in H_2-reduced Fe-MIL-101 for enhanced Fenton-like degradation of organic pollutants. *J. Hazard. Mater.* **441**, 129922 (2023).
27. Z. Gan, Z. Xiao, Z. Zhang, Y. Li, C. Liu, X. Chen, Y. Liu, D. Wu, C. Liu, X. Shuai, Y. Cao, Stiffness-tuned and ROS-sensitive hydrogel incorporating complement C5a receptor antagonist modulates antibacterial activity of macrophages for periodontitis treatment. *Bioact. Mater.* **25**, 347–359 (2023).
28. W. Zhu, J. Mei, X. Zhang, J. Zhou, D. Xu, Z. Su, S. Fang, J. Wang, X. Zhang, C. Zhu, Photothermal nanozyme-based microneedle patch against refractory bacterial biofilm infection via iron-actuated Janus ion therapy. *Adv. Mater.* **34**, e2207961 (2022).
29. D. D. Zhang, Ironing out the details of ferroptosis. *Nat. Cell Biol.* **26**, 1386–1393 (2024).
30. H. Pi, R. Sun, J. R. McBride, A. R. S. Kruse, K. N. Gibson-Corley, E. S. Krystofiak, M. R. Nicholson, J. M. Spraggins, Q. Zhou, E. P. Skaar, Clostridioides difficile ferrosome organelles combat nutritional immunity. *Nature* **623**, 1009–1016 (2023).
31. J. M. Skerker, B. S. Perchuk, A. Siryaporn, E. A. Lubin, O. Ashenberg, M. Goulian, M. T. Laub, Rewiring the specificity of two-component signal transduction systems. *Cell* **133**, 1043–1054 (2008).
32. Z. Zhong, S. Zhou, Y. Liang, Y. Wei, Y. Li, T. Long, Q. He, M. Li, Y. Zhou, Y. Yu, L. Fang, X. Liao, B. N. Kreiswirth, L. Chen, H. Ren, Y. Liu, J. Sun, Natural flavonoids disrupt bacterial iron homeostasis to potentiate colistin efficacy. *Sci. Adv.* **9**, eadg4205 (2023).
33. Y. Huang, X. Wan, Q. Su, C. Zhao, J. Cao, Y. Yue, S. Li, X. Chen, J. Yin, Y. Deng, X. Zhang, T. Wu, Z. Zhou, D. Wang, Ultrasound-activated piezo-hot carriers trigger tandem catalysis coordinating cuproptosis-like bacterial death against implant infections. *Nat. Commun.* **15**, 1643 (2024).
34. H. Dai, Q. Fan, C. Wang, Recent applications of immunomodulatory biomaterials for disease immunotherapy. *Exploration* **2**, 20210157 (2022).
35. X. Hu, J. Chen, S. Yang, Z. Zhang, H. Wu, J. He, L. Qin, J. Cao, C. Xiong, K. Li, X. Liu, Z. Qian, 3D printed multifunctional biomimetic bone scaffold combined with TP-Mg nanoparticles for the infectious bone defects repair. *Small* **20**, 2403681 (2024).
36. H. Wu, H. Dong, Z. Tang, Y. Chen, Y. Liu, M. Wang, X. Wei, N. Wang, S. Bao, D. Yu, Z. Wu, Z. Yang, X. Li, Z. Guo, L. Shi, Electrical stimulation of piezoelectric BaTiO3 coated Ti6Al4V scaffolds promotes anti-inflammatory polarization of macrophages and bone repair via MAPK/JNK inhibition and OXPHOS activation. *Biomaterials* **293**, 121990 (2023).
37. P. Wu, L. Shen, H.-F. Liu, X.-H. Zou, J. Zhao, Y. Huang, Y.-F. Zhu, Z.-Y. Li, C. Xu, L.-H. Luo, Z.-Q. Luo, M.-H. Wu, L. Cai, X.-K. Li, Z.-G. Wang, The marriage of immunomodulatory, angiogenic, and osteogenic capabilities in a piezoelectric hydrogel tissue engineering scaffold for military medicine. *Mil. Med. Res.* **10**, 35 (2023).
38. Y. Zhao, Y. Zhu, J. Zhu, H. Wang, Z. Ma, L. Gao, Y. Liu, K. Yang, Y. Shu, J. He, Atomic-resolution investigation of structural transformation caused by oxygen vacancy in $La_{0.9}Sr_{0.1}TiO_{3+\delta}$ titanate layer perovskite ceramics. *J. Mater. Sci. Technol.* **104**, 172–182 (2022).
39. D. Tai, B. Li, H. Xue, T. Zheng, J. Wu, $BiFeO_3$-$BaTiO_3$ ferroelectrics: Decrypting the mechanism of rare earth doping-induced electrical property discrepancy via scaling behavior and multi-level structure. *Acta Mater.* **262**, 119411 (2024).
40. W. Li, Y. Ma, T. Feng, Z. Du, Y. Liu, S. V. Kalinin, J.-F. Li, Q. Li, Delineating complex ferroelectric domain structures *via* second harmonic generation spectral imaging. *J. Mater.* **9**, 395–402 (2023).
41. X. Du, X. Guo, Z. Gao, F. Liu, F. Guo, S. Wang, H. Wang, Y. Sun, X. Tao, Li_2MTeO_6 (M=Ti, Sn): Mid-infrared nonlinear optical crystal with strong second harmonic generation response and wide transparency range. *Angew. Chem. Int. Ed. Engl.* **60**, 23320–23326 (2021).
42. X. Zhou, Z. Wang, Y. K. Chan, Y. Yang, Z. Jiao, L. Li, J. Li, K. Liang, Y. Deng, Infection micromilieu-activated nanocatalytic membrane for orchestrating rapid sterilization and stalled chronic wound regeneration. *Adv. Funct. Mater.* **32**, (2022).
43. Z. Yang, X. Fu, D. Ma, Y. Wang, L. Peng, J. Shi, J. Sun, X. Gan, Y. Deng, W. Yang, Growth factor-decorated Ti_3C_2 MXene/MoS_2 2D bio-heterojunctions with quad-channel photonic disinfection for effective regeneration of bacteria-invaded cutaneous tissue. *Small* **17**, e2103993 (2021).
44. M. M. Vijatović Petrović, J. D. Bobić, A. M. Radojković, J. Banys, B. D. Stojanović, Improvement of barium titanate properties induced by attrition milling. *Ceram. Int.* **38**, 5347–5354 (2012).
45. Y.-C. Wang, J. M. Wu, Effect of controlled oxygen vacancy on H_2-production through the piezocatalysis and piezophototronics of ferroelectric R3C $ZnSnO_3$ nanowires. *Adv. Funct. Mater.* **30**, (2020).
46. W. Hu, L. Lin, R. Zhang, C. Yang, J. Yang, Highly efficient photocatalytic water splitting over edge-modified phosphorene nanoribbons. *J. Am. Chem. Soc.* **139**, 15429–15436 (2017).
47. S. Wu, J. Xu, L. Zou, S. Luo, R. Yao, B. Zheng, G. Liang, D. Wu, Y. Li, Long-lasting renewable antibacterial porous polymeric coatings enable titanium biomaterials to prevent and treat peri-implant infection. *Nat. Commun.* **12**, 3303 (2021).
48. H. Peng, D. Wang, D. Ma, Y. Zhou, J. Zhang, Y. Kang, Q. Yue, Multifunctional yolk–shell structured magnetic mesoporous polydopamine/carbon microspheres for photothermal therapy and heterogenous catalysis. *ACS Appl. Mater. Interfaces* **14**, 23888–23895 (2022).
49. Y. Li, Q. Ran, Q. Duan, J. Jin, Y. Wang, L. Yu, C. Wang, Z. Zhu, X. Chen, L. Weng, Z. Li, J. Wang, Q. Wu, H. Wang, H. Tian, S. Song, Z. Shan, Q. Zhai, H. Qin, S. Chen, L. Fang, H. Yin, H. Zhou, X. Jiang, P. Wang, 7-Dehydrocholesterol dictates ferroptosis sensitivity. *Nature* **626**, 411–418 (2024).
50. M. A. Kohanski, J. J. Collins, Rewiring bacteria, two components at a time. *Cell* **133**, 947–948 (2008).
51. Y. Kong, F. Liu, B. Ma, J. Duan, W. Yuan, Y. Sang, L. Han, S. Wang, H. Liu, Wireless localized electrical stimulation generated by an ultrasound-driven piezoelectric discharge regulates proinflammatory macrophage polarization. *Adv. Sci.* **8**, 2100962 (2021).
52. G. Kresse, D. Joubert, From ultrasoft pseudopotentials to the projector augmented-wave method. *Phys. Rev. B* **59**, 1758–1775 (1999).

53. J. P. Perdew, K. Burke, M. Ernzerhof, Generalized gradient approximation made simple. *Phys. Rev. Lett.* **77**, 3865–3868 (1996).
54. S. Grimme, J. Antony, S. Ehrlich, H. Krieg, A consistent and accurate ab initio parametrization of density functional dispersion correction (DFT-D) for the 94 elements H-Pu. *J. Chem. Phys.* **132**, 154104 (2010).

Acknowledgments: We thank L. Li, F. Chen, C. Bao, and Y. Deng (Institute of Clinical Pathology, West China Hospital) for processing histological staining; L. Wu, Q. Shi, Y. Wu, and J. Tu (Core Facility of West China Hospital, Sichuan University) for the help with Imaris image analysis, confocal microscopy, and micro-CT; M. Zhang (College of Polymer Science and Engineering, Sichuan University) for TEM micrographs; and L. Chai, Y. Li, X. Xu, and W. Gao (Core Facility of West China Hospital, Sichuan University) for the technical assistance. **Funding:** This work was supported by the following: National Natural Science Foundations of China (nos. 82472402 and 82102542 to D.W. and no. 82172394 to Z.Zho.), the Sichuan Science and Technology Program (nos. 2023YFQ0039 and 2023ZYD0070 to D.W.), National Key Research and Development Program of China (nos. 2022YFC2503100 and 2022YFC2503104 to Z.Zho.), 1.3.5 project for disciplines of excellence, West China Hospital, Sichuan University (nos. ZYGD23033 and 2023HXFH012 to Z.Zho.), and Mianyang Science and Technology Bureau (no. 2022ZYDF087 to Q.S.). **Author contributions:** Conceptualization: F.Z., X.L., and D.W. Methodology: X.W., Y.Z., Q.L., Y.Y., Z.Zha., X.C., L.T., J.C., and S.L. Investigation: F.Z., H.X., Q.S., and L.Z. Visualization: F.Z. Supervision: X.T., J.W., X.Y., J.L., and Z.Zho. Writing—original draft: F.Z. and X.W. Writing—review and editing: F.Z., X.W., X.L., and D.W. **Competing interests:** The authors declare that they have no competing interests. **Data and materials availability:** All data needed to evaluate the conclusions in the paper are present in the paper and/or the Supplementary Materials.

Submitted 1 September 2024
Accepted 21 January 2025
Published 14 March 2025
10.1126/sciadv.ads8694